FAILURE ANALYSIS OF THE TYPE 304 STAINLESS STEEL 4-in.
RECIRCULATION BYPASS LINES OF THE MONTICELLO BWR POWER PLANT*

by

S. Danyluk, J. Y. Park, and C. F. Cheng

ARGONNE NATIONAL LABORATORY
9700 South Cass Avenue
Argcnne, Illinois   60439

Materials Science Division

April 1976

Table of Contents

Table of Contents (Contd.)

List of Figures

List of Tables

FAILURE ANALYSIS OF THE TYPE 304 STAINLESS STEEL 4-in.
RECIRCULATION BYPASS LINES OF THE MONTICELLO BWR POWER PLANT*

by

S. Danyluk, J. Y. Park, and C. F. Cheng

SUMMARY

The intergranular cracking observed in the Type 304 stainless steel
4-in. recirculation bypass lines of the Northern States Power Company (NSP)
Monticello power plant is similar to that observed in other boiling-water-
reactor (BWR) systems. These failures are attributed to intergranular stress-
corrosion cracking (ISCC). Contributing factors are: local variations in
water chemistry, changes in the metallography of the heat-affected zone (HAZ)
as a result of welding, and localized tensile stresses.

Two types of defects were discovered in the initial examination of the
4-in. line. A major crack, was located in the HAZ of weld RBBJ-10. It
was determined to be 90% through the wall. It followed the circumference
of the pipe, and is intergranular in nature. Shallow crack-like defects
were also found at the weld root. These were both intergranular and
transgranular. All the defects initiated at the inside diameter (ID) surface.

The influence of sensitization on crack initiation and propagation is
not firmly established. A sensitization test showed that the major crack
was not in an area of maximum sensitization; this crack was 0.32 in.
from the weld, and the maximum sensitization was 0.5 in. from the weld. Trans-
mission-electron-microscope (TEM) examination showed that precipitates are
present in the grain boundaries in the vicinity of the major crack. It is
not known how these precipitates affect the grain-boundary energy and/or
influence crack propagation.

Tensile stresses in the HAZ are required for ISCC to occur. These stresses are a result of residual stresses from ID surface preparation (e.g., machining) and weld shrinkage and externally applied loads such as fit-up stresses, dead weight, thermal expansion, and pressure. In other BWR systems, grinding was assumed to be a major contributor to the cracking problem since it would greatly increase residual stresses. However, in the present system the ID surfaces were machined. Since the correlation between machining and residual stress has not been established, the magnitude of this stress is not known. The stress analysis of Loops A and B, including cold springing and dead weight, showed that large stresses were present at the elbows and joints. Residual-stress measurements have shown that cracks in the 4-in. line are in a region of maximum tensile stress (0.3 in. from the weld root).[1] These stresses, which result from weld shrinkage, add to the externally applied loads. Metallurgical and geometric factors also affect the tensile stresses. Variation (∼10%) in pipe wall thickness was measured within the HAZ. Recrystallization at the ID surface due to (a) surface deformation by mechanical working and (b) the weld heat input, provides localized areas at the grain boundaries for crack initiation.

The water chemistry at the crack tip and at localized regions (pits) of the ID surface is not known. Monitoring of the reactor water and feed water did not show unusual chemical constituents. The radioactivity of the pipe was high; higher than Dresden-II and Quad Cities-II piping. It has been speculated that component radioactivity is closely tied to the corrosion properties of the surface.[2] Active ions are thought to diffuse to the pores of the oxide film and become incorporated into the oxide structure. Thus, monitoring of the corrosion-product activity may provide information on the corrosion rate.

After the work on weld RBBJ-10 was completed, additional data (x-ray) became available which showed that circumferential and axial defects may be present in other welds of the 4-in. line. A metallographic examination of these defects was not made.

I. Introduction

On January 20, 1975, during in-service inspection, linear indications were detected by ultrasonic testing (UT) in two welds in Loop A and one weld in Loop B of the Monticello BWR recirculation system 4-in.-diam bypass lines. A refueling outage was in progress at the time. Radiographic examination of these three welds verified the UT results in one of these welds. The radiographs indicated circumferential cracking in the weld HAZ. No obvious explanations that would account for the cracks were apparent, but it appeared that the cracks were similar in nature to those observed in the Millstone, Dresden-II, Quad Cities-I and II, Fukushima, and Peach Bottom-III BWRs.

The sections of Loops A and B that contained the suspected cracks were removed and shipped to Argonne National Laboratory (ANL) for metallurgical examination. The present report is a summary of the failure analysis conducted at ANL.

II. Description of 4-in. Line and In-service Environmental Conditions

A. Geometry

Boiling-water reactors have two 28-in. recirculation lines. The 4-in. lines bypass a 28-in. gate valve in the recirculation lines. A schematic of the pressure vessel and recirculation system is shown in Fig. 1. The bypass lines supply reactor coolant water to warm the 28-in. header before the recirculation pump is started and relieve the pressure on the gate valve in

the 28-in. line. Detailed schematics of the 4-in. bypass lines of the Monti-
cello plant are shown in Figs. 2 (Loop A) and 3 (Loop B). The bypass valves
shown in these figures remained open during reactor operation, contrasting
with the Dresden and Quad Cities plants, which operated with the bypass
valves closed. The weld locations are noted in the figures and are labeled,
e.g., RBAJ-9. The water flow proceeds as indicated. The welds suspected
of having defects are RBAJ-8, RBAJ-7, RBAJ-6, and RBBJ-10. The hanger
positions are also labeled.

B. Material and Welding Procedure

All the piping is Schedule 80, Type 304 stainless steel. The elbows are
of the same heat of material as are the pipes, although they have been subjected
to additional heat treatments in the forming process (hot bending). The trans-
mission electron micrographs suggest that the elbow was not completely solution-
ized after forming.

The exact welding procedure is not available but welding was conducted
according to the ASME Nuclear Code, Section IX. The open-root technique of butt
welding was employed using the tungsten-inert-gas and shielded-metal arc
processes. The joints were prepared with a 70° minimum fit-up angle, and the
ID surfaces were counterbored. The beveled edges, root face, and back side of
each weld joint were cleaned prior to welding. Certified ER308 and E308-15
filler metal was used with a specified maximum interpass temperature of 350°F.
Argon was used for torch shielding, and purge gas.

C. Vibration Analysis, Water Chemistry, and Radioactivity

A test program to monitor the pipe displacement and discharge pressure
fluctuations was conducted by the Bechtel Power Corporation. Pressure trans-
ducers were mounted on an instrument line outside the drywell and connected
with 1-in. tubing to the recirculation system piping. Acceleration data were
collected by a portable accelerometer that measured the vibration of the 4- and
28-in. lines. Data were collected as the pump speed and motor power were
varied. It was found that the dynamic amplitudes were small (<1 mil) and

?requencies were lower than 12.5 Hz. Turbulence in the line results in
pressure fluctuations as the pump motor speed is increased. The Bechtel
report concluded that the combination of low vibration amplitude and low
frequency presented no hazard to the bypass-line integrity and that "it is
better to operate with the bypass valve open,"[3] as had been standard practice
in the Monticello plant.

The water chemistry in the bypass line is not monitored. However, the
feed water and reactor water are monitored for pH, conductivity, chlorides,
solids, and metals. The results of the reactor-water chemistry analysis
showed the following: chlorides <10 ppb, silicates 170-200 ppb, ^{131}I iodine
0.16 μCi/ml, and pH between 6.5 and 8.5. A feed-water oxygen level of 50 ppb
and a conductivity of 0.1 μmho were also measured. The results are within
the BWR operating-condition limits.

The radioactivity of the pipe was measured at ANL under three different
conditions: as received, after soaking in a solvent (NS-1*) for 100 h at
250°C, and after ultrasonic cleaning. The results of the β-, γ-, and α-activity
are shown in Table I. The solvent and ultrasonic cleaning conditions removed
the loose corrosion scale from the ID surface of the pipe so that metallurgical
investigation could proceed without undue precautions. The α-activity is a
result of fuel-element leakage during reactor operation.

III. Examination of Pipe

As a result of the failure analyses performed at ANL on other Type 304 stain-
less steel piping (Dresden units I and II and Quad Cities-I and II)[5] a flexible,
specific program of data acquisition that has proven useful for identification
of the nature of the cracking has been developed. The program calls for: field

---

*Proprietary decontamination solution of Dow Chemical Company, Nuclear Industrial
Service.[4]

nondestructive examination (NDE), water chemistry analysis, stress measurements, corrosion-product sampling, recording of cold springing, cutting and packaging to prevent ID surface contamination, decontamination of activity by rinsing, and laboratory investigation that involves NDE, corrosion-product analysis, and metallographic and electron microscopy. Various aspects of the analysis performed on the Monticello bypass piping are discussed below.

A. Defective Pipe Removal and Nondestructive Examination

The defective pipe sections were removed from the plant with a motorized hack saw. The cuts were made under "dry" conditions (no lubricant), and the pipe ends covered with polyet' 'lene sheet after cutting to prevent ID surface contamination. The inventory of pipe, included three 90° elbows, one 45° elbow, and one straight piece, as shown in the Appendix. Nondestructive examinations were conducted on all the pipe welds received by ANL.

These examinations included single-wall radiographic, ultra-sonic (shear wave only), and dye penetrant methods. The radiographs were taken with a source-to-film distance of 43 in., with the film mounted in conventional flexible cassettes. The ultrasonic examination was conducted using a conventional hand-held scan (2.25-MHz, 1/4 x 1/4-in., 45° shear-wave transducer). The amplitude sensitivity was calibrated by means of a flat piece of 0.600-in.-thick Type 304 stainless steel with a 20% wall-thickness rectangular notch. No artificial damping or rejection threshold levels were used. The gain of the instrument was set to yield 80% of full-scale deflection when the ultrasonic signal reflects from the 20% wall-thickness notch. During scanning the gain was increased 12 dB. A dye-penetrant exam..ation that employed Magnaflux Zyglo was performed using standard techniques.

The results of the UT and radiographs for the nine welds investigated are shown in Figs. 4 and 5. These figures are schematics of the unfolded pipe with the weld root separating the pipe and elbow sections. The numbers at the

top of the figure denote the clock positions. Ultrasonic test indications
are present on both the elbow and pipe sides of the weld; however, it is not
possible to determine the orientation of the indications due to geometric masking
of the UT signal. Radiographic indications appear on the pipe side of the
weld at all the joints except RBAJ-8 and RBAJ-9. The latter two welds have
radiographic indications on both sides of the joint. Dye penetrant examination
of the radiographic indications located in welds RBBJ-12, RBAJ-9, RBAJ-8
and RBAJ-6 did not confirm the presence of cracking in these joints.

Prior to in-depth laboratory radiography of all welds, it had been de-
cided that weld RBBJ-10 would be subjected to a detailed metallographic
examination. Preliminary field ultrasonic examination had indicated the
presence of a significant defect in this joint. Subsequent field radiography
had verified the presence of a crack.

Further metallographic exploration of indications located through ultra-
sonic or radiographic examinations of welds other then RBBJ-10 is not planned.

B. Crack Verification

Upon receipt at ANL, the sections were scrubbed with a clean nylon brush
and distilled water, on both outside and inside surfaces, for removal of loose
radioactive contamination. Corrosion product was taken from the ID surface
near weld RBAJ-8 by scraping and analyzed by x-ray powder diffraction.

Weld RBBJ-10 was cut from the pipe using a motorized hack saw and included
~1/2-in. of material on each side of the weld bead. The elbow geometry is shown
in Fig. 6a. Figure 6b shows a three-dimensional view of the weld and the ob-
served major crack, which extends from the 7 1/4 to the 8 3/4 clock position.

Two weld-root defects were also observed. The ID surface of the pipe is shown in Fig. 7a with the weld bead and defects. The elbow side of the weld is toward the top of the figure. A higher-magnification photograph is shown in Fig. 7b. The major crack can be seen on the pipe side of the weld bead. The major crack follows the circumference and jogs along the counterbored machine marks. The weld-root defects are visible in Fig. 7b.

Figure 8 is a cross-sectional view of the weld that shows the extent of crack penetration. It is clear from the figure that the crack has initiated at the ID surface and has penetrated at least 90% through the wall. Also visible in the figure is an inclusion in the weld (center).

C. Macroscopic and Microscopic Investigation

1. Macroscopic and Metallographic Examination

A composite cross-sectional metallographic view of the major crack is shown in Fig. 9. Sample preparation included metallographic polishing prior to etching in a 10% oxalic acid solution using a current density of 1 A/cm^2 to delineate the grain boundaries. Several interesting features in this figure are worth noting. The crack is intergranular, and dark irregular-shape areas, which may have contained precipitates or grains, are evident. Branching of the main crack is also readily seen.

A cross-sectional view of the crack-like defects at the weld root is shown in Fig. 10. These typical weld-root defects, which have blunt tips, occur on both sides of the weld. The grain size of the base material on the pipe side differs from that of the elbow side because of the mechanical working and heat treatment received by the elbow during the forming (hot bending) process. The grain size in the bulk of the elbow material is larger than at the ID surface. This difference (Fig. 11) is partially due to the forming process and the heat provided during welding. Figure 11b, which is a magnified view of Fig. 11a,

shows surface "pitting," the preferential attack at the grain boundaries possibly due to the use of NS-1 decontamination solution.

The weld was sectioned as shown in Fig. 8, and the crack was opened to reveal the fracture surface. Figure 12 shows a three-dimensional schematic with the sectioning geometry and major crack location. Figure 13 shows the two mating pieces after the major crack shown in Fig. 12 had been opened. The regions labeled A and B were cut using a cutoff wheel with a silicon carbide blade. The crack front separates the high contrast region from the intergranular cracked region. Care was exercised not to disturb the crack front such that, after sawing, the sample was cooled to liquid nitrogen temperatures and the crack was opened by impact fracture.

2. SEM Examination

The fracture surface of the major crack was subjected to scanning-electron-microscope (SEM) examination after removal of the oxide scale; the surface was then gold shadowed and reexamined. The oxide was removed by exposure of the fracture surface to the NS-1 solution (250°C for 100 h). The effectiveness of this solution for removing the oxide scale has been the subject of a recent study[6] in which it appears that the interface between the oxide and the base metal is preferentially attacked. The grain boundaries of the base metal are also attacked such that precipitates which may have been present are dissolved away. The effects of the decontamination solution are seen by comparing Figs. 14a and 14b. These photos show the morphology of the surface after ∼100 (Fig. 14a) and 219 h (Fig. 14b) in the decontamination solution. "Tongue" behavior, fine slivers of metal usually found on cleavage facets, is apparent in these figures. It has been shown that such features result from plastic deformation (cleavage across microtwins) at the tip of the main propagating crack.[7] The fracture-surface morphology is shown in Fig. 15,

where the unremoved oxide scale (bright areas) is also visible. The high-contrast regions, indicative of oxide charging due to electron-beam bombarding, made high-resolution microscopy difficult. Gold shadowing of the fracture surface resolved this problem by providing a thin conducting layer, which leaked accumulated charge away. A disadvantage of this technique is that the chemistry of the original surface is changed such that quantitative chemical information is lost. The observation of slip on individual grains was common, and some examples are shown in Figs. 16 and 17. Also shown in Fig. 17 is a case of branching-crack arrest at the intersection of three grain boundaries. Transgranular fracture of some grains was also observed, as shown in Fig. 18.

Figure 19 shows the ID surface at which the crack initiated. Also visible in the figure are pits that formed possibly during pickling when the material was fabricated. These pits are seen both at the center of the grain and at the grain boundaries.

The main crack branched during propagation. A characteristic of these branches is "clean" grain-boundary separation. A typical branched crack is shown in Fig. 20. Also seen in this figure are precipitates, which appear as bright contrast areas embedded in the grains, and dark circular areas from which these precipitates have been removed.

The SEM study showed that the crack is predominantly intergranular, with some transgranular fracture also occurring. Twinning cleavage fracture and slip were identified but could not be attributed to fatigue. Pitting of the ID surface was also observed; however, a direct correlation to crack initiation has not been made.

3. TEM Examination

Transmission-electron microscopy was performed on three thin disks (numbered 1, 3, and 4 in Fig. 21) punched from the HAZ near the weld. Disks 3 and 4 were adjacent to the major crack. The grain boundaries were examined

in each case. Photographs of these grain boundaries are shown in Figs. 22-24, which display bright- and dark-field views. Care was taken to expose any precipitates that may have been present. The micrographs show discontinuous precipitates in position 1, a few traces of precipitates in position 3, and no precipitates in position 4. The precipitates, usually identified as $M_{23}C_6$ carbides, are thought to contribute to ISCC. The presence of precipitates on the elbow side suggest that the solutionizing treatment was not complete. Continuous precipitates were not observed in these samples. It must be noted, however, that the small number of grain boundaries examined does not represent a statistically significant sample. Additional TEM studies are required to correlate the suscept-ibility of this material to ISCC with precipitates at grain boundaries.

D. Quantitative Chemical Analysis

1. Corrosion Products

The loose and adherent corrosion products at the ID surfaces were analyzed by the x-ray powder-diffraction technique using $CuK\alpha$ and $FeK\alpha$ radiation. The adherent corrosion products were removed by light mechanical scraping before cleaning and washing. Table II lists the types of oxide scale found in the Monticello plant pipe and their relative x-ray line intensity. Results from Quad Cities-III and Dresden-II are included for comparison.

In general, no significant difference in corrosion products exists among the three reactors, and no unusual products are found. Spinels of nickel ferrite and nickel chromite are tightly bound to the surface substrate. The hematite (α-Fe_2O_3) is probably a redeposition product from the oxygen-rich region in the core that results from radiolytic decomposition of water. In the case of Quad Cities-III the hematite is probably converted licombite, which results from scrubbing with trisodium phosphate. The austenite is likely to have resulted from metal dissolution, whereas kamacite may originate from transformed martensite at the machine-disturbed metal surface or from debris due to galling and wear.

2. X-ray-dispersive Analysis

X-ray-dispersive analysis was performed on the precipitate particles and substrate material. The x-ray intensities (CuKα radiation) are shown in Figs. 25 and 26. Chromium, iron, nickel, and silicon are present in both the precipitate and substrate; however, sulfur is observed only in the precipitate. Differences in peak height are readily seen and have previously been attributed to oxide spinels.[8]

3. Sensitization

The degree of sensitization in the HAZ was examined using ASTM A262 Practice A. This procedure is a rapid means of determining whether austenitic stainless steel is susceptible to intergranular attack. A cross section of the weldment shown in Fig. 8 was polished (3/0 final polish) and etched in a 10-wt% solution of oxalic acid for 1.5 min at a current density of 1 A/cm^2. The acid preferentially attacks carbides, which, in a sensitized stainless steel, have precipitated at the grain boundaries. Thus, the etched structure may be used to approximate the degree of sensitization. The results from the above procedure are shown in Fig. 27. The series of photographs in the figure show the weldment (Fig. 27a) and successive 0.1-in. intervals along the axial direction of the pipe (Figs. 27b-h). Variations in grain-boundary etching are readily observed, with the maximum occurring ∼0.5 in. from the weld fusion line. Deformation lines parallel to the direction of the pipe axis are visible in Figs. 27f-h and are the result of the pipe fabrication (extrusion) process.

A quantitative measure of the degree of sensitization, i.e., the degree of grain-boundary etching by oxalic acid, was obtained by measuring the ratio of the area of etched grain boundaries to the total surface area, as obtained from the photographs of Fig. 27. These results, obtained with the IMANCO QUANTIMET 720, are plotted in Fig. 28. In addition to the maximum sensitization,

~0.5 in. from the weld fusion line, a crack is shown at ~0.3 in. The background signal, due to the deformation lines, has increased the apparent value of sensitization at large distances from the weld fusion line. The true sensitization reading should be much lower and decrease to zero as the distance is increased.

E. Wall-thickness Measurement and Stress Analysis

1. Circumferential Wall-thickness Measurement

Wall-thickness measurements around the circumference were taken 1/8 in. from the fusion line of weld RBAJ-7. The results, shown in Fig. 29, are plotted as wall thickness versus angular position. It is apparent that significant thickness changes, which could lead to stress concentrations, may be present in the HAZ as a result of weld shrinkage. Weld shrinkage may also lead to cold cracks due to tensile stresses. It may be assumed that measurements for the other welds will show similar variations in thickness.

2. Stress Analysis of Cold Springing and Dead Weight

Stresses in piping may reach values close to or in excess of yield. These stresses arise from externally applied loads such as dead weight of the pipe, operating fluid pressure, thermal stresses induced at the operating temperatures, fit-up stresses imposed during plant assembly, and residual stresses locked into the microstructure by cold work and weld shrinkage. Each effect adds to the bending, axial, and hoop stresses and shear stress due to torsion.

Residual stresses near the welds have not been measured. However, these measurements are being conducted as part of an ongoing program sponsored by the Electric Power Research Institute (EPRI). The results are not available to date.

A stress analysis of both the A and B loops that included cold springing, dead weight, pressure, and temperature measurements was performed. The

cold springing of both loops is shown in Fig. 30, with numbers indicating straight-line pipe segments (elements). Loop A was severed at the junction of elements 3 and 4, and the measured separations were 1/2 in. along the pipe axis and 3/8 in. perpendicular to the axis. The cold springing of Loop B, measured at the junction of elements 4 and 5, was 1/2 in. along the pipe axis. The stresses were calculated assuming a three-dimensional beam analysis, with the flexibility of the elbows being neglected. Also, the 4-in. pipe section was assumed to be connected at both ends to immovable supports. The analysis is done by inputting the geometry and external constraints into the SAP IV Pipe Bend Element Code. The output of this code is fed into the IBM SSP subroutine SIMQ, where the unknown loads are calculated. The stresses are computed by dividing the loads by the moment areas. The results of the analysis, considering cold bending alone, are shown in Tables III and IV, which include maximum bending stress (σ_B), uniform axial stress (σ_T), and shear stress due to torsion (τ). The beam-type loads due to pressure have been neglected because of their small value. Since the bypass valve on both 4-in. lines was in the open position, the temperature difference between the 4- and 28-in. line is assumed small; nsequently, stresses imposed by thermal expansion have also been neglected. The results listed in the tables show that (a) high stresses are present at the connection between the 4- and 28-in. lines and are distributed through a weld-o-let and (b) the stresses are distributed through the other welds, with certain welds showing higher stresses than others. For example, welds RBBJ-9, RBBJ-10, and RBBJ-11 show a relatively higher stress than the other welds in Loop B.

The stresses due to dead weight have also been computed, and the results are shown in Tables V and VI. The variation in stress for the welds can be seen. The stresses in Loop B were higher than those in Loop A. A conservative estimate of the cumulative effect of dead weight and cold spring

stresses can be ma 'e by simply adding the values at each weld.

We believe the absolute magnitudes of the quoted stresses are not in themselves especially significant because of the simplifying assumption made in the analysis, although the relative values of stress may be significant. The stresses due to cold springing and dead weight will, of course, add to the residual stresses and may contribute to the conditions for crack initiation.

F. ID Surface Examination

The ID surface of weld RBBJ-10 was examined for unusual surface-preparation marks and weld shrinkage. Figure 31 shows the ID surface near the crack. The crack edge and fracture surface are seen at the left of the figure. Machine marks are clearly seen in the center of the field of view and are recognizable because of their regularity. The surface preparation at the weld root is seen in Fig. 32. Figure 32a shows the machining marks due to counterboring (at the left) and precipitates embedded in grain boundaries. The weld-root crack is also shown (cross-sectional view in Fig. 10) and solidification marks can be seen at the right of the figure. A higher-magnification photograph of the crack is shown in Fig. 32b. The crack follows the weld root but not necessarily the grain boundaries. It is surmised that this crack is the result of weld shrinkage which led to tensile stresses at the ID surface and is not a stress-corrosion crack.

IV. Discussion

The factors that cause ISCC of stainless steels in BWR systems have been discussed in detail by various authors.[9] No single cause has been found to predominate either in the crack initiation or crack propagation aspects of ISCC. It seems clear, however, that ISCC is promoted by environmental effects such as the chemistry of the water in contact with the steel, micro-

structural effects at the surface as well as the bulk of the matrix, and/or stress effects which result from residual stresses left by cold working or weld shrinkage.

We proceed with a discussion of these three aspects as they pertain to the present failure analysis.

A. Environmental Effects

The role that chemical impurities and temperature play in ISCC in BWR systems has not been established. However, it has been suggested that primary water lines of pressurized-water reactors (PWRs) which contain oxygen of <0.1 ppm do not show intergranular cracking.[10] Concentrations of oxygen in the Monticello plant feedwater were continuously monitored and showed a value of <50 ppb, although concentrations in the 4-in. lines and crevices and notches at the pipe surface may be substantially different. Large increases of the oxygen level in the plant water have also been reported.[11] These occurred during plant shutdown; however, direct correlation with ISCC has not been determined to date. The transport of other impurities through the water has been reported in PWR plants, and it was suggested that these may play a role in the failure-initiation stage of ISCC.[12] Unusual chemical activity has not been identified in the water nor in the material.

B. Microstructural Effects

The relation of microstructure to ISCC in BWR systems is not clearly understood. The grain size, degree of sensitization, and surface cold working all contribute to some extent to ISCC in Type 304 stainless steel. Sensitization is caused by precipitation at the grain boundaries of chromium carbides and/or compounds that contain Mn, P, S, Si, and N. The cracks do not, however, form in the regions of highest precipitation but in areas that are only lightly sensitized. The 4-in. lines of Dresden, Quad Cities, and Monticello all developed cracks at ~0.3 in. from the weld fusion line (a region of light

sensitiz..ion). The role that sensitization plays in crack initiation has
not been firmly established. The TEM results presented in Figs. 22-24 show
the discontinuous nature of the precipitates on the pipe side of the weld
near the crack region. Areas examined farther from the weld showed grain
boundaries without precipitates. The SEM results revealed precipitates on
the fracture surface that may fracture in a brittle manner and weaken the
grain boundary, thus providing an easy path for crack propagation and material
dissolution. The main crack exhibited features of slip, grain-boundary
separation, crack arrest, cleavage, and transgranular fracture. These effects
indicate that the plastic deformation of individual grains had occurred as
the crack propagated but corrosion also was taking place. Pits were observed
at grain bou.daries and at the centers of grains (Fig. 19) and may be due to
pickling during pipe fabrication. The association of pits with crack-initiation
sites was made, but no direct evidence has been found.

The effects of cold work and recrystallization combine to change the
grain size at the ID surface of the pipe. The correlation of grain size with
ISCC has not, however, been established.

C. Stress Effects

Stress is necessary for the repeated rupture of the passivating oxide
film and subsequent electrochemical dissolution of the metal in the de-
passivated areas. The possible sources of stress are: cold fit-up of the
pipe joints prior to welding, hangar-imposed stresses at the operating
temperatures, dead weight, pressure, and mechanical cold working of the pipe
surface, which leads to residual stresses. Increases in the surface stress may be
caused by thickness differences due to pipe weld shrinkage, surface roughness
from machining during weld preparation, postweld cleanup, and pickling pits.
Stress levels approaching yield are possible if all the effects that increase
the stress are accounted for.

Measurements of the cold springing at room temperature were used to calculate the stresses in the weld joints. The stresses are nominally small, although values of 10 ksi (Table IV) have been calculated. The addition of the dead weight and cold springing stresses shows values of approximately half the yield stress. Examination of Tables III-VI and Figs. 4 and 5 reveals that the welds which show the strongest UT and radiograph indications are those with the highest stress values. Weld RBBJ-10 showed a maximum in stress; welds RBAJ-6, RBAJ-7, and RBAJ-8 also showed a high stress level and UT and radiograph indications. Residual stresses have not been measured for the present report but are being measured under the sponsorship of EPRI. The pipe thickness of weld RBAJ-7 varied by 10%; this variation would change the stress by the same percentage.

The ID surfaces of the pipe were counterbored (machined). It has been speculated by other authors[1] that surface deformation leads to residual stresses and grinding is a more severe surface preparation procedure than machining. It seems clear that the stress induced in the surface regions of the pipe will depend on the metal removal rate and the force used in the removal process. In the present case these variables are unknown. Additional insight into the present problem may be gained from the residual-stress measurements.

Weld shrinkage was evident (Figs. 31 and 32) from the crack-like defects observed at the weld root. The nature of these defects is different from that of the intergranular crack which was examined metallographically. Weld shrinkage will induce stresses in the HAZ that will add to the externally applied loads.

Fatigue striations due to alternating stress levels were not observed. Slip was quite evident in many of the grains (Figs. 16 and 17), and the corners of grains had undergone plastic deformation. The accelerometer tests performed by Bechtel Corporation showed that dynamic amplitudes were small (<1 mil) and of low frequency (<12 Hz). However, low-amplitude and low-cycle tension-tension stresses may not produce striations and these effects have not been ruled out.

Acknowledgments

References

1. C. F. Cheng, W. A. Ellingson, D. S. Kupperman, J. Y. Park, R. B. Poeppel, and K. J. Reimann, "Corrosion Studies of Nuclear Piping in BWR Environments," Quarterly Report for the Quarter Ending June 30, 1975, Argonne National Laboratory, prepared for the Electric Power Research Institute under contract #31-109-38-3138L.

2. D. H. Lister, "The Transport of Radioactive Corrosion Products in High Temperature Water-I. Recirculating Loop Experiments," Nucl. Sci. and Eng. 58, 239 (1975).

3. J. R. Darnell and S. W. Giampapa, "Dynamic Test Report-Reactor Recirculation Bypass Line Test-Monticello Generating Station," Bechtel Power Corporation, January 1975, prepared for the Northern States Power Company.

4. D. E. Harmer, F. P. Fauson, M. A. Snyder, O. U. Anders, and J. J. Holloway, "Developing a Solvent, Process, Equipment and Procedures for Decontaminating the Dresden-1 Reactor," presented at the 37th Annual Meeting of the American Power Conference, Chicago, Illinois, April 1975.

5. Craig F. Cheng, "Failure Analyses for Cracked Type 304 Stainless Steel Piping in the 4-in. Recirculation Bypass Lines of the Dresden-II and Quad Cities-II BWR Systems," Argonne National Laboratory, December 1974, prepared for the Commonwealth Edison Company.

6. C. F. Cheng, unpublished.

7. Metals Handbook, Vol. 9, "Fractography and Atlas of Fractographs," 8th Edition, American Society of Metals, Metals Park, Ohio, 1975.

8. Craig F. Cheng and Edward E. Potter, Nucl. Met. 19, 273 (August 1973).

9. Proc. Symp. on Materials Performance in Operating Nuclear Systems, CONF-730801, Nucl. Met. 19 (August 1973).

10. Craig F. Cheng, J. Nucl. Mater. 56, 11 (1975).

11. J. Danko, presented at the meeting on BWR Pipe Cracking, O'Hare Hilton Hotel, Chicago, March 4, 1975, sponsored by the Electric Power Research Institute.

12. T. E. Rummery, 5th Canadian Seminar on Surfaces, University of Laval, Quebec, Canada, June 1-3, 1975.

Table I

Radioactivity

	$\beta + \gamma$ @ 1 in. (mr/h)	γ @ 1 in. (mr/h)	α[a] (DPM/cm^2)
As-received ID surface	290	50	984 (1180)[b]
NS-1 solvent (250°F, 100 h)	38	2	498
Ultrasonically cleaned after NS-1 solvent (250°F, 100 h)	0.3	0.1	<1

[a]Dry smear. The α energies were found for the following:
Pu^{239} and/or Pu^{240}; Am^{241} and/or Pu^{238}; Cm^{242}, possibly Cf^{252};
and Cm^{244}.

[b]Chemical dissolution method.

Table II

Corrosion Products in the 4-in. Recirculation Bypass Lines
(Monticello, Quad Cities-III, and Dresden-II)[a]

	Monticello		Quad Cities-III Loop A		Dresden-II Loop A	Loop B
	Loose Product	Scrubbed[b] ID	Loose Product	Scrubbed[c] ID	As-received ID	As-received ID
Spinel ($NiFe_2O_4$ + $NiCr_2O_4$)	A	S	M	M	M	M
Hematite (α-Fe_2O_3)	S	M	A	A	M	W
Kamacite (α-Fe, BCC)	W	W	W	W	S	W
Austenite (γ-Fe, FCC)	S	W	S	S	S	S
Ciprite (Cu_2O)	A	A	A	A	W	A
Lipcombite $Fe_3(PO_4)_2)OH)_2$	A	A	M	W	A	A

[a]Relative x-ray intensity of oxide scale: S = strong, M = medium, A = absent, and W = weak.

[b]Deionized water scrubbed.

[c]Trisodium phosphate scrubbed.

Table III

Results of Stresses Due to Cold Springing in Loop A

Weld Identification Number[a] (RBAJ-)	σ_B	σ_T	τ
weld-o-let	8000	–	-2800
13	7200	–	-2800
12	100	–	-4400
11	100	–	-4400
10	4400	–	–
Cut 1	150	–	–
9	2400	–	–
8	2400	-150	100
7	2800	-150	100
6	2100	-100	-1000
weld-o-let	5700	-100	-1000

[a]From Figs. 2 and 3.

Table IV

Results of Stresses Due to Cold Springing in Loop B

Weld Identification Number (RBBJ-)	σ_B	σ_T	τ
weld-o-let	12,300	-	1200
17	3,800	-	1200
23	4,400	700	-400
13	2,200	700	-400
12	7,900	200	1030
10	9,900	200	1030
9	10,100	700	-
Cut 2	600	700	-
8	600	700	-
7	400	700	230
weld-o-let	33,000	200	230

Table V

Results of Stresses Due to Dead Weight in Loop A

Weld Identification Number (RBAJ-)	σ_B	σ_T	τ
weld-o-let	500	400	500
13	400	400	500
12	3200	50	1500
11	3000	50	1500
10	4100	-	-
Cut 1	1400	-	-
9	900	-	-
8	400	-100	400
7	3500	-300	400
6	3500	-300	300
weld-o-let	1000	-400	300

Table VI

Results of Stresses Due to Dead Weight in Loop B

Weld Identification Number (RBBJ-)	σ_B	σ_T	τ
weld-o-let	3200	-	1900
17	600	-	1900
16	3700	-80	-
13	2000	-80	-
12	1700	30	-
10	4300	-60	-
9	4200	-80	-
Cut 2	2600	-80	-200
8	3500	-80	-200
7	3500	200	-100
weld-o-let	3000	-400	-100
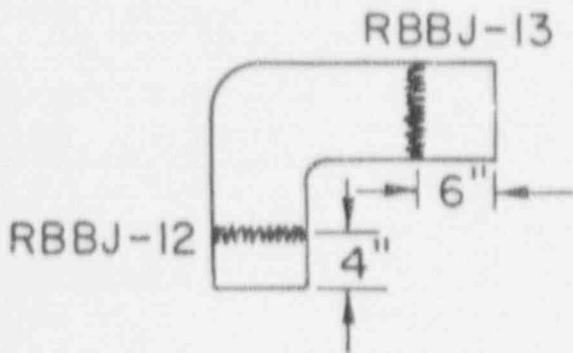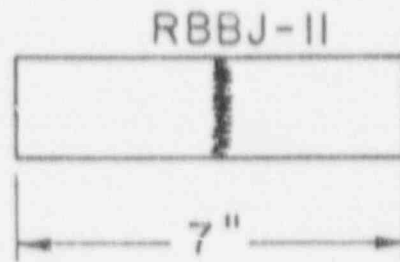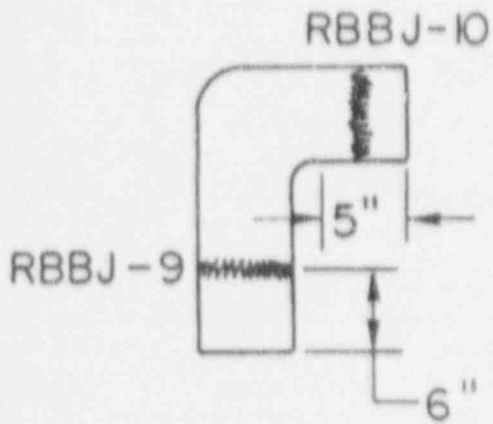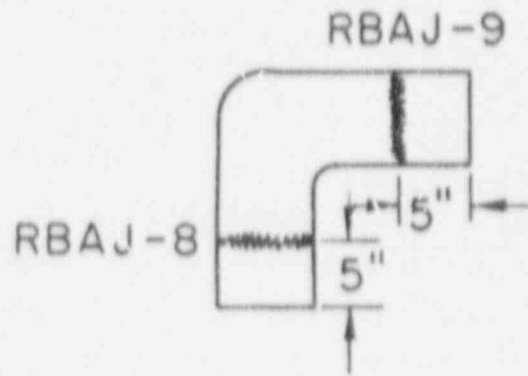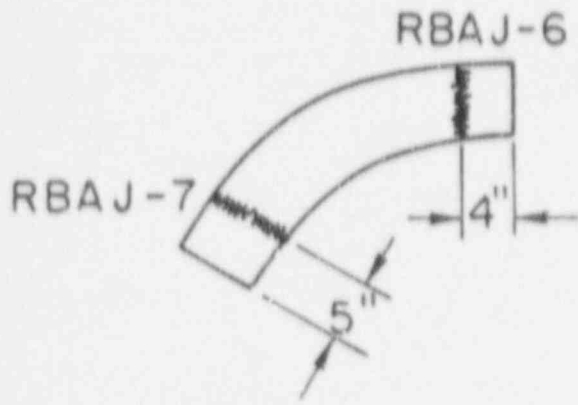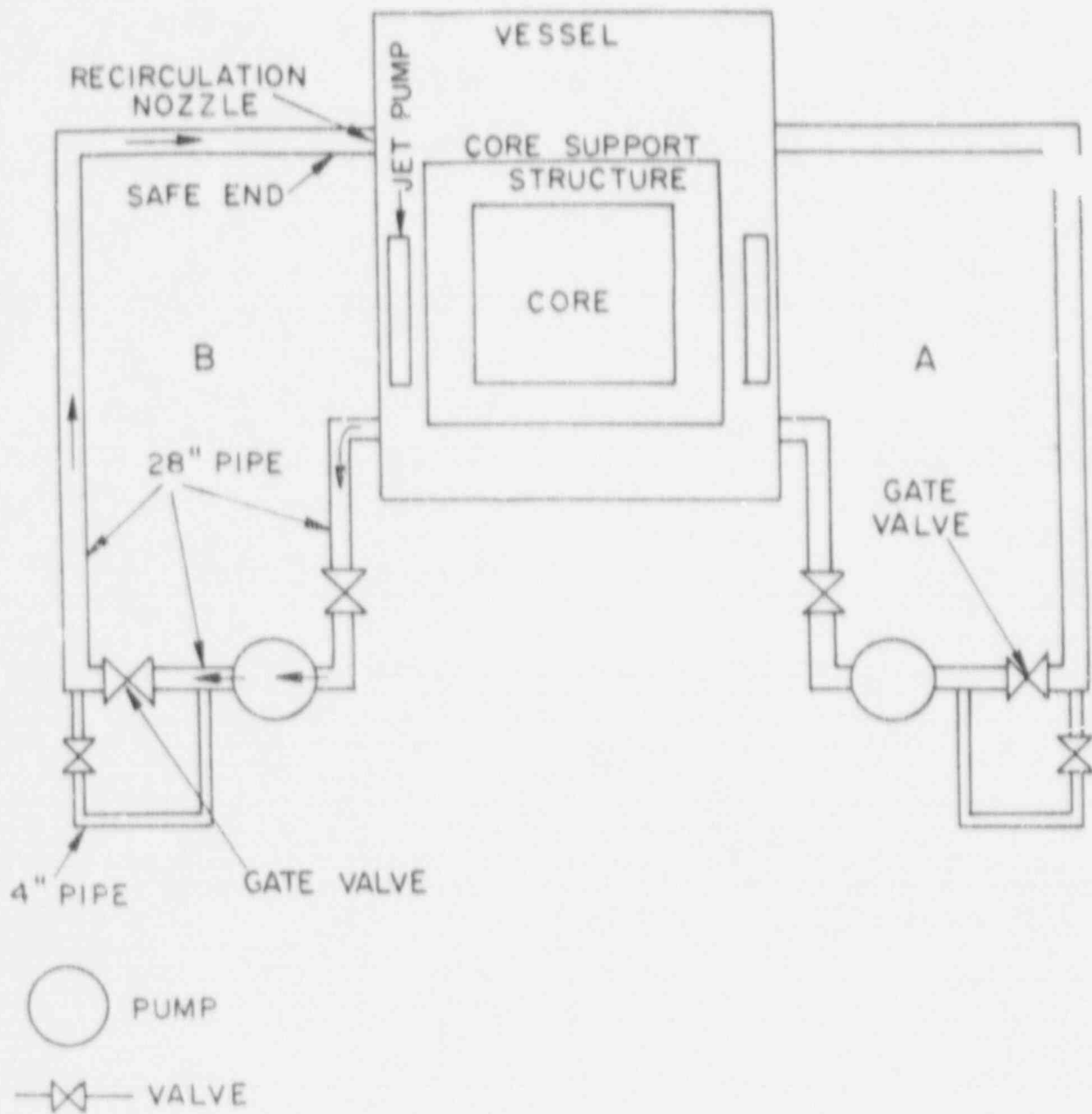
Fig. 1. Schematic showing the BWR water loop system. The 4-in. lines are indicated along with the gate valves and water flow direction.
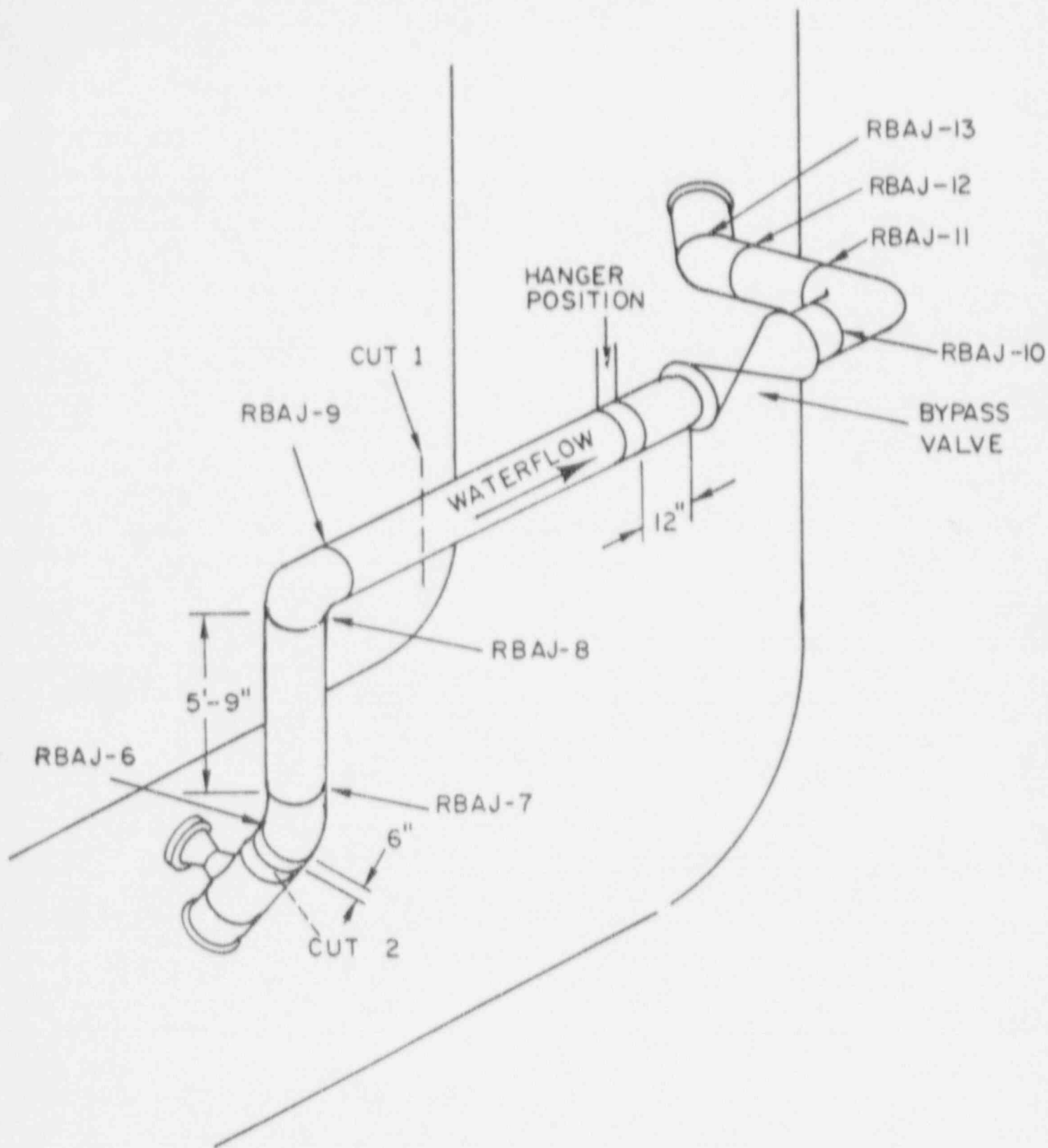
Fig. 2. Loop A of the 4-in. recirculation bypass line. The weld locations and bypass valve are indicated. Water flow proceeds as shown. The cuts are also shown along with the hangar location and cold springing.
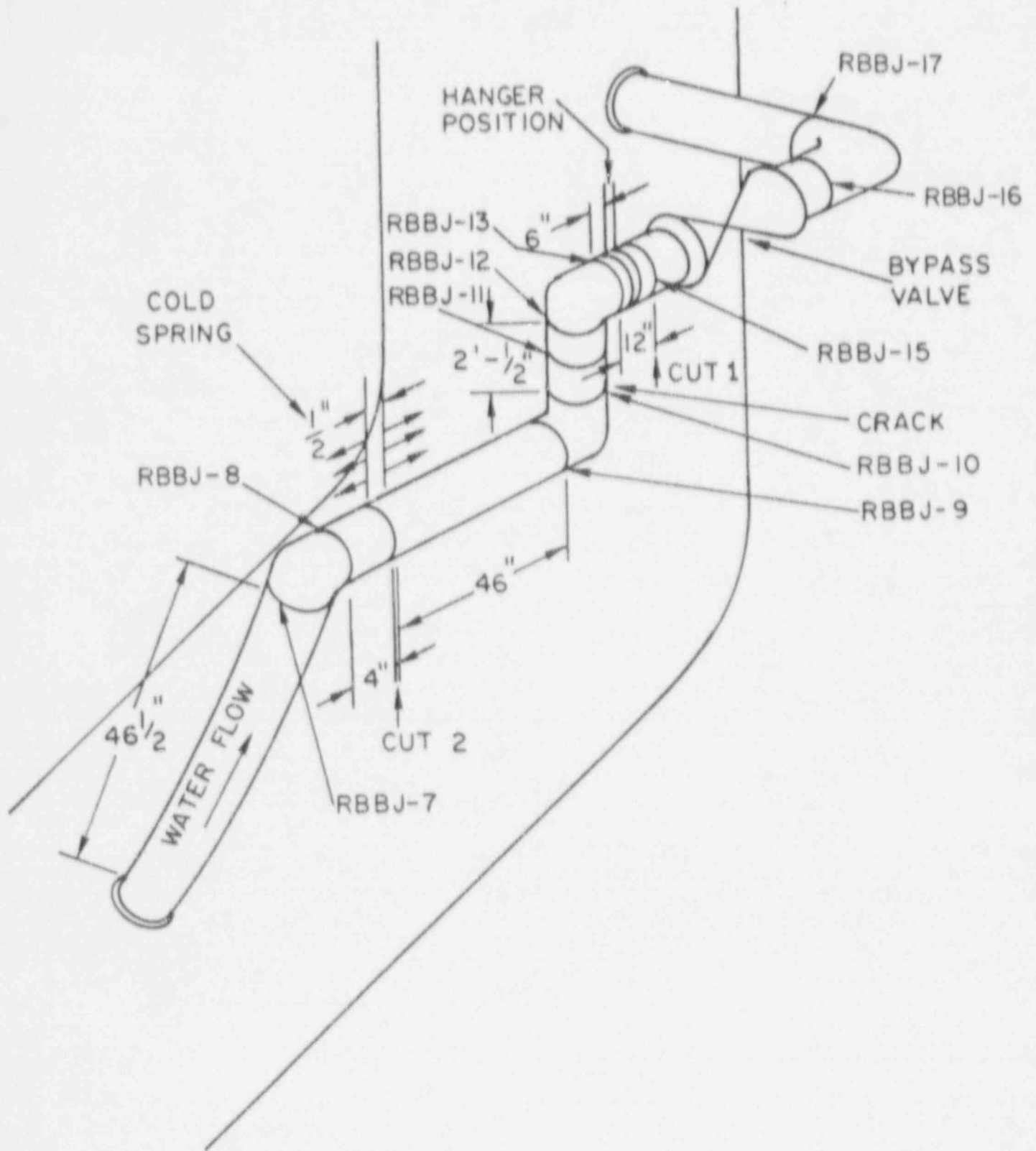
Fig. 3. Loop B of the 4-in. recirculation bypass line. The weld locations, bypass valve, and water flow are shown. The cuts are shown along with the hangar location and cold springing.
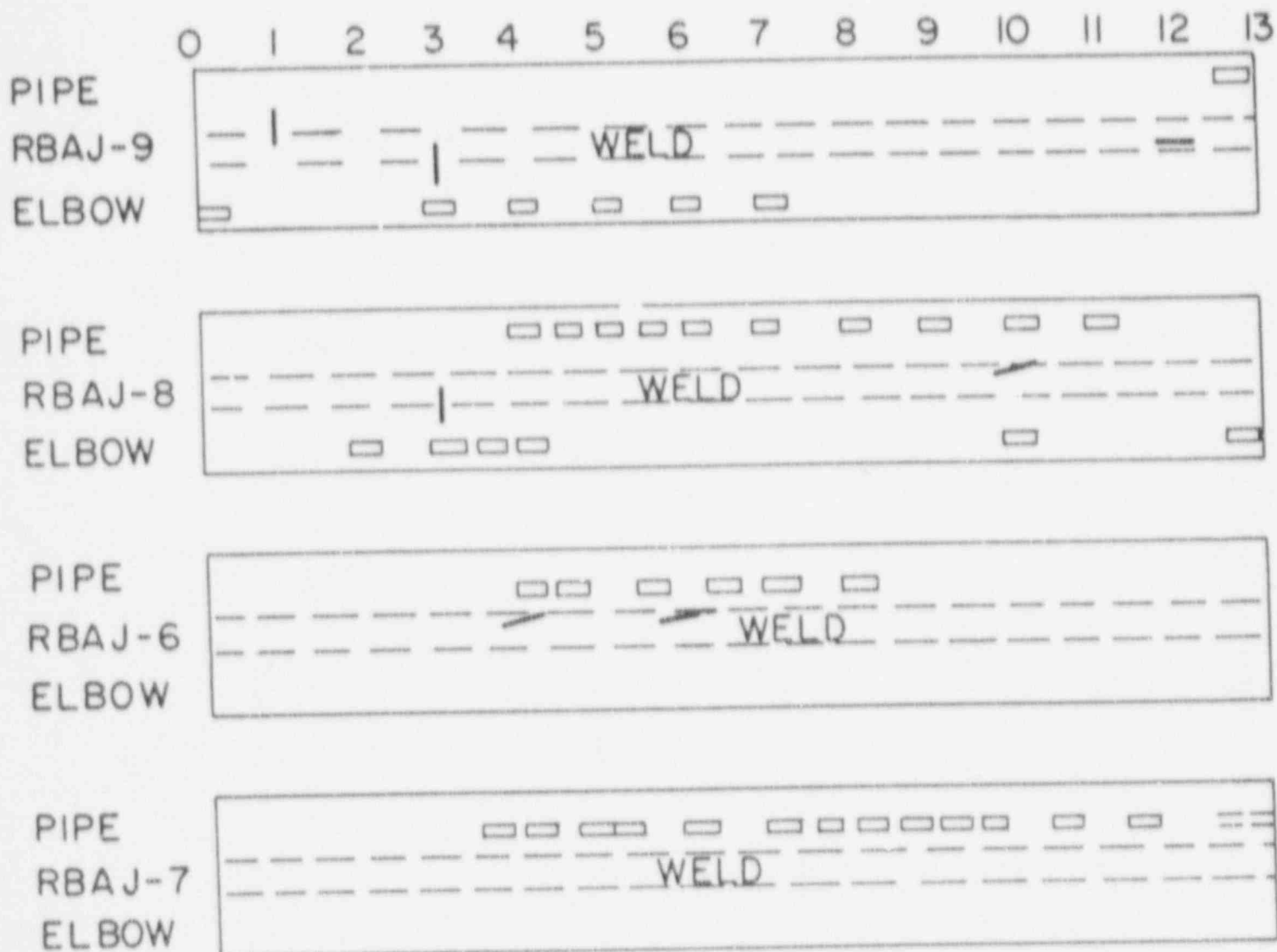
Fig. 4. Radiograph and ultrasonic results of welds from Loop A. The figure is an axial unfolding of the pipe with the weld shown at the center of each diagram and the clock positions numbered at the top. The view is from the pipe OD. The pipe and elbow sides of the weld are also shown.
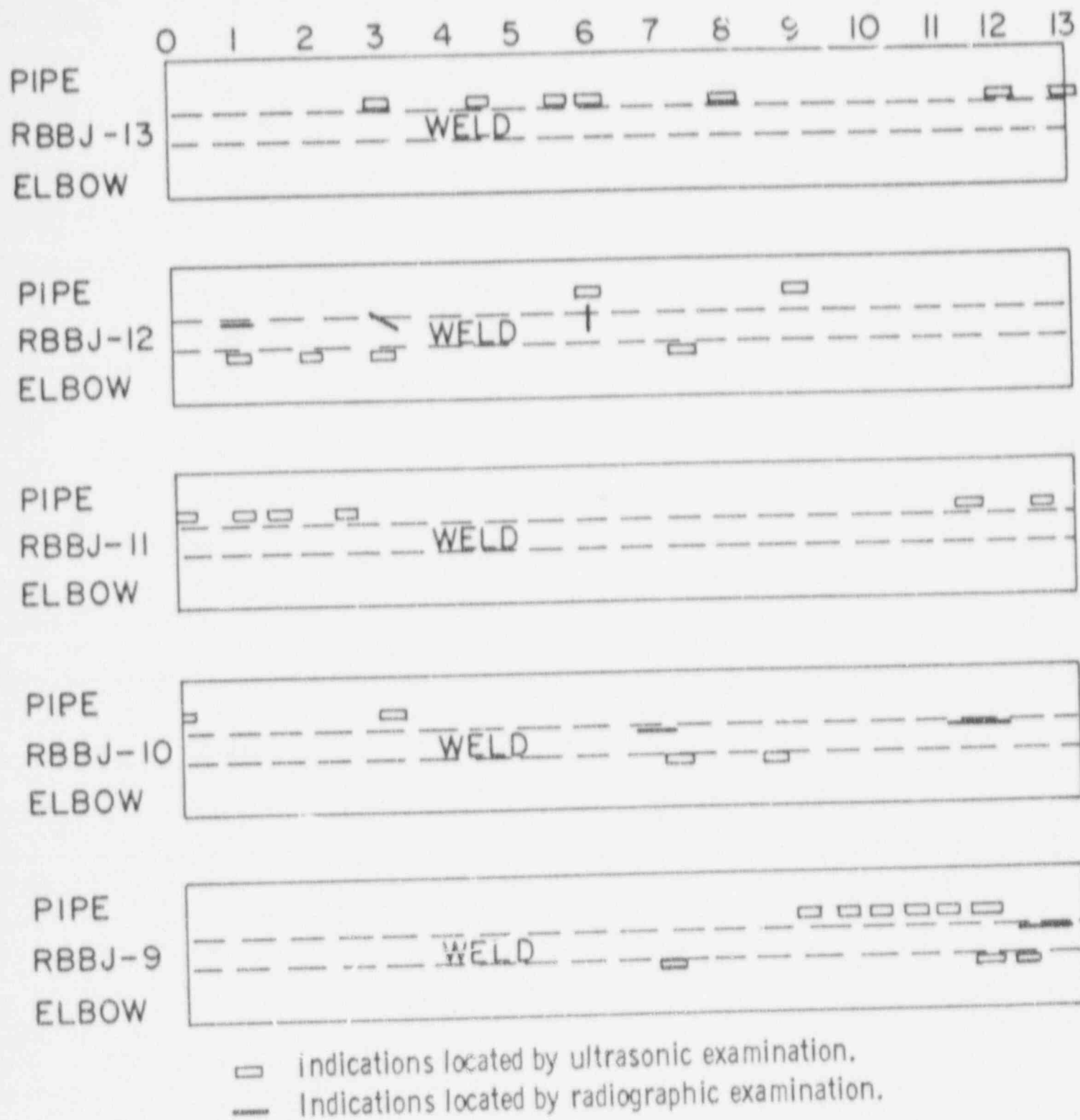
Fig. 5. Radiograph and ultrasonic results of welds from Loop B. The figure is an unfolding of the pipe with the weld shown at the center of each diagram and the clock positions numbered at the top. The pipe and elbow sides of the weld are also shown.
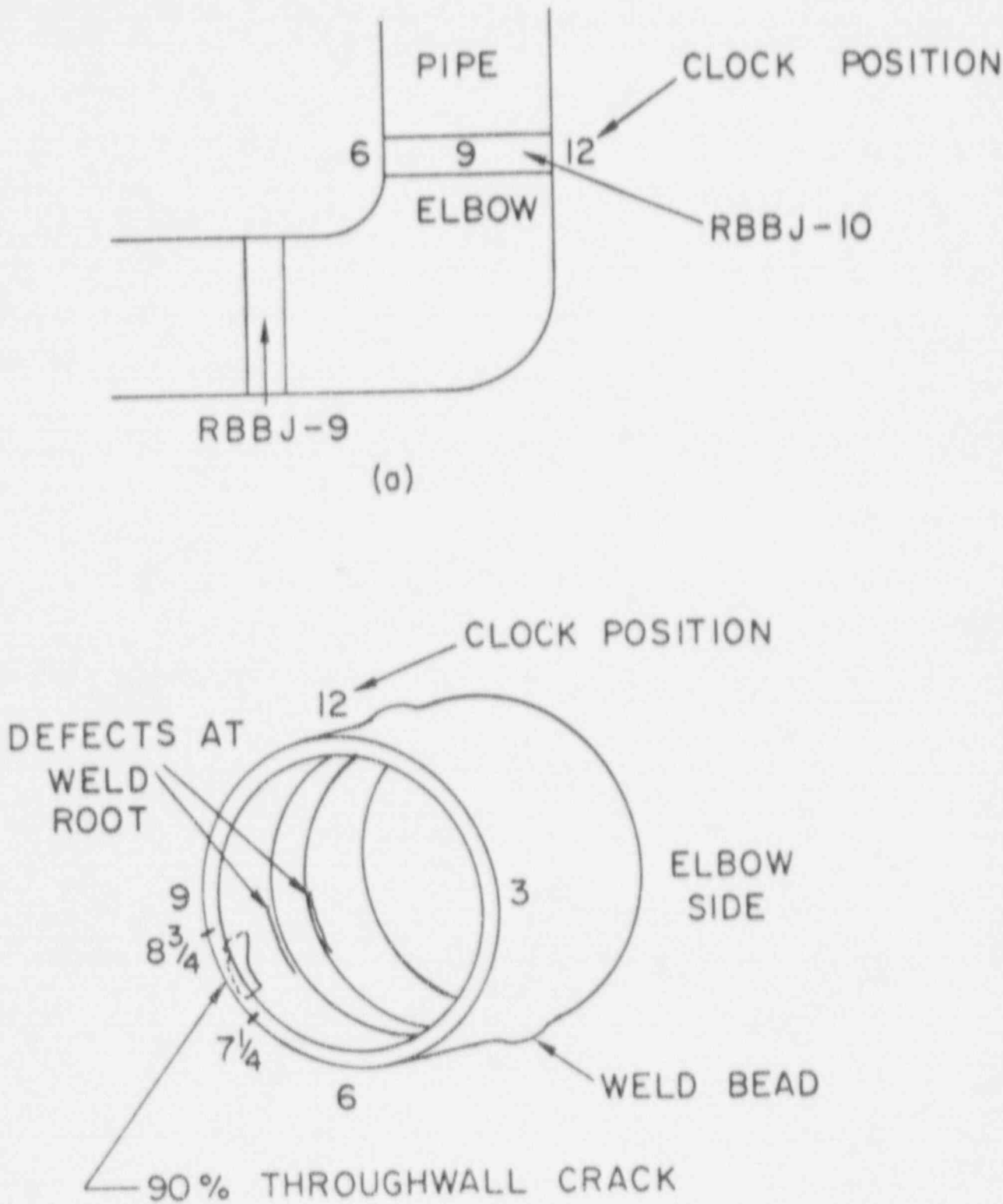
Fig. 6. (a) Schematic of Loop B with the elbow containing welds RBBJ-9 and RBBJ-10. The clock positions are shown. (b) A three-dimensional schematic showing weld RBBJ-10. The weld bead and clock positions are shown. The defects were located at the 7 1/4 to 8 3/4 clock position. One (90% throughwall) crack was observed in the HAZ, and two defects were detected at the weld root.
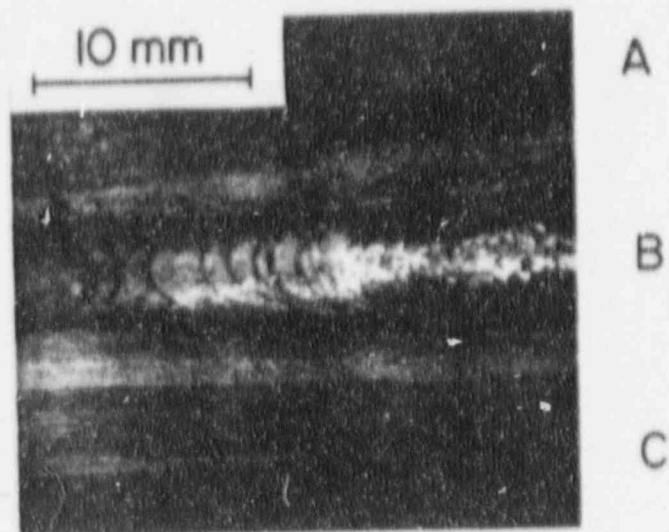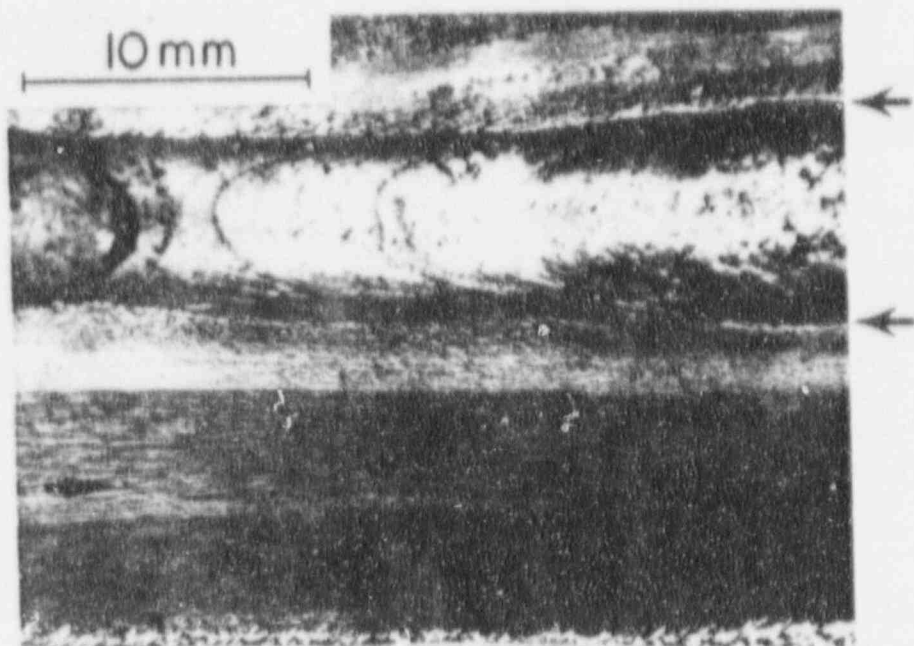
Fig. 7. (a) The ID surface of weld RBBJ-10. The weld bead (B) and elbow (A) and pipe (C) sides of the weld are indicated. The clock positions are 8 3/4 at the left and 7 1/4 at the right. (b) A higher-magnification photo of (a). The machining marks at the surface are readily seen. The major crack and two surface defects are visible (arrows).

ELBOW SIDE

PIPE SIDE

10mm
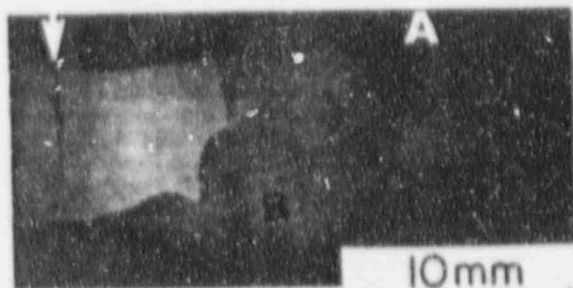
Fig. 8.   A cross-sectional view of weld RBBJ-10. The crack (arrow) penetrated 90% throughwall after it had originated at the ID surface (A). A weld imperfection is also visible (B).
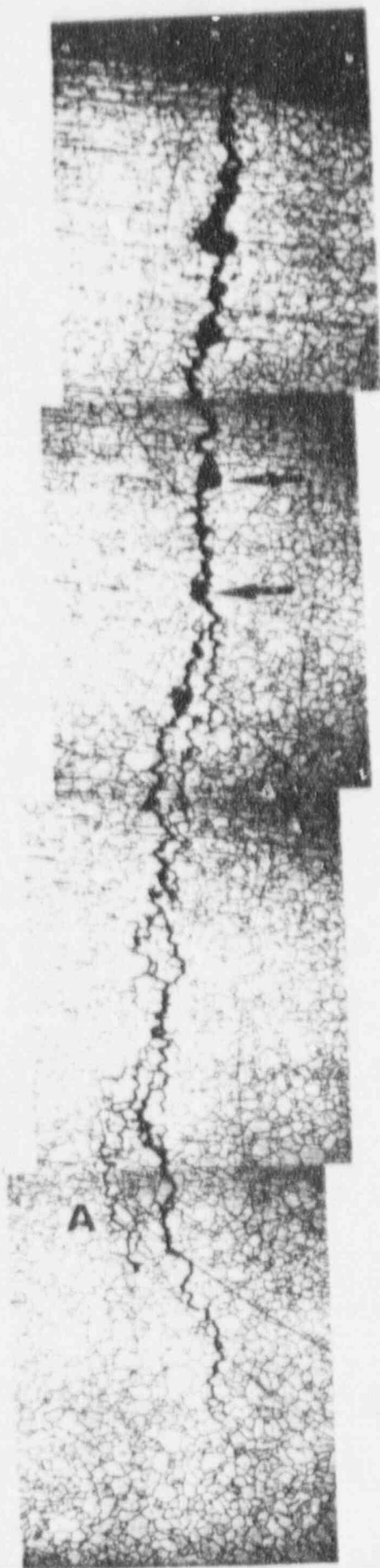
Fig. 9. An enlarged view of the crack in the HAZ. An oxalic acid etch was used to delineate the grain boundaries. The dark irregular-shape areas (arrow) may have contained grains and/or precipitates. Crack branching is also observed.

1 mm
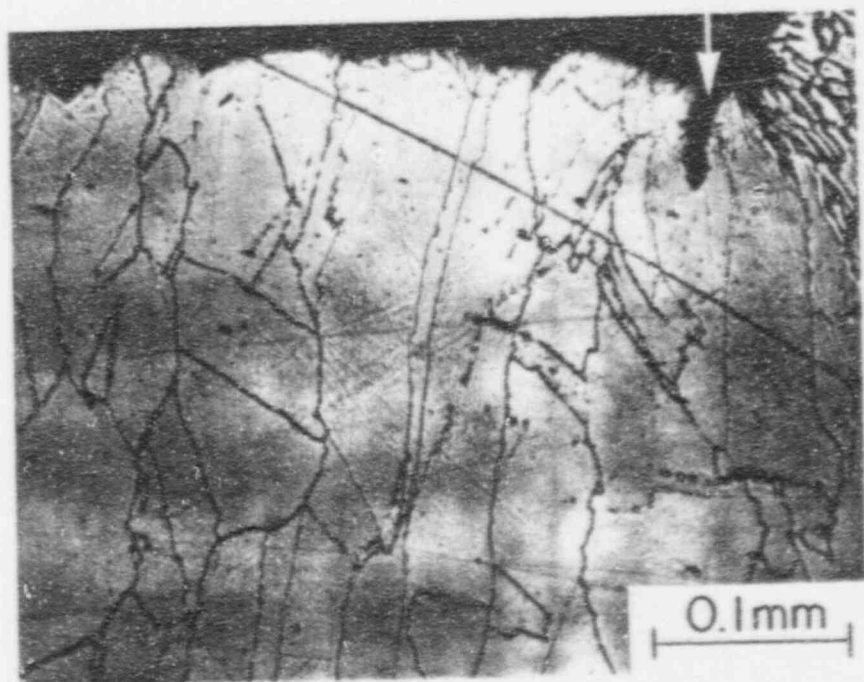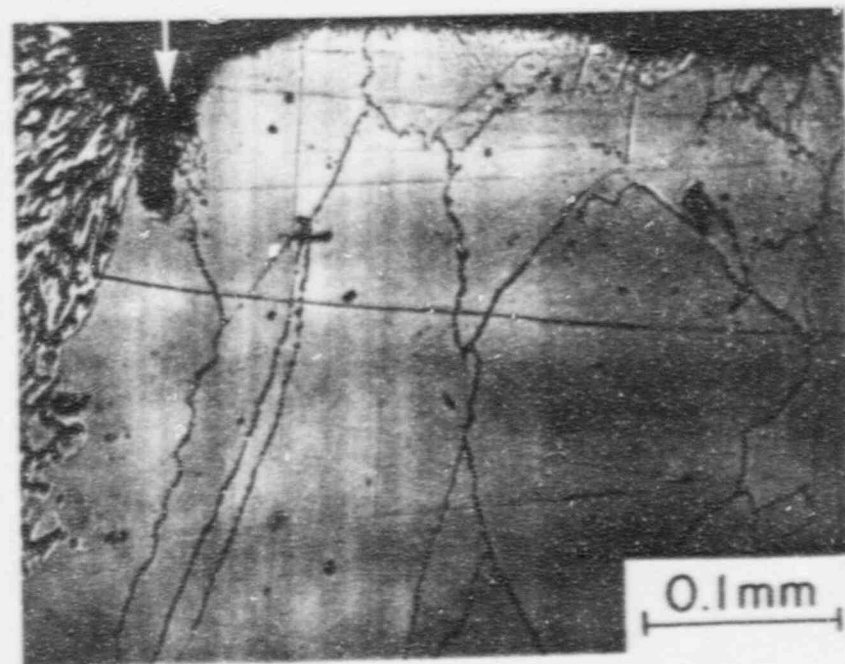
Fig. 10. The defects at the weld root are shown at the pipe side (A) and elbow side (B) of the weld. These crack-like defects are shallow (0.004") and transgranular and have blunted tips. This type of defect in this location has not contributed to the (BWR) piping failures investigated at ANL. The grain size differences are attributed to the thermal history of the elbow.
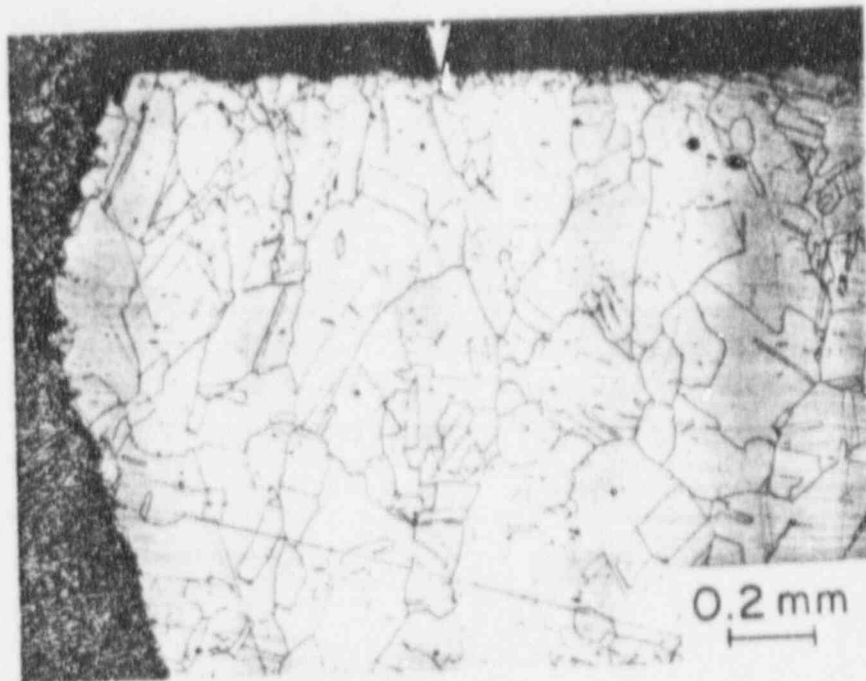
WELD-FUSION
LINE   (a)
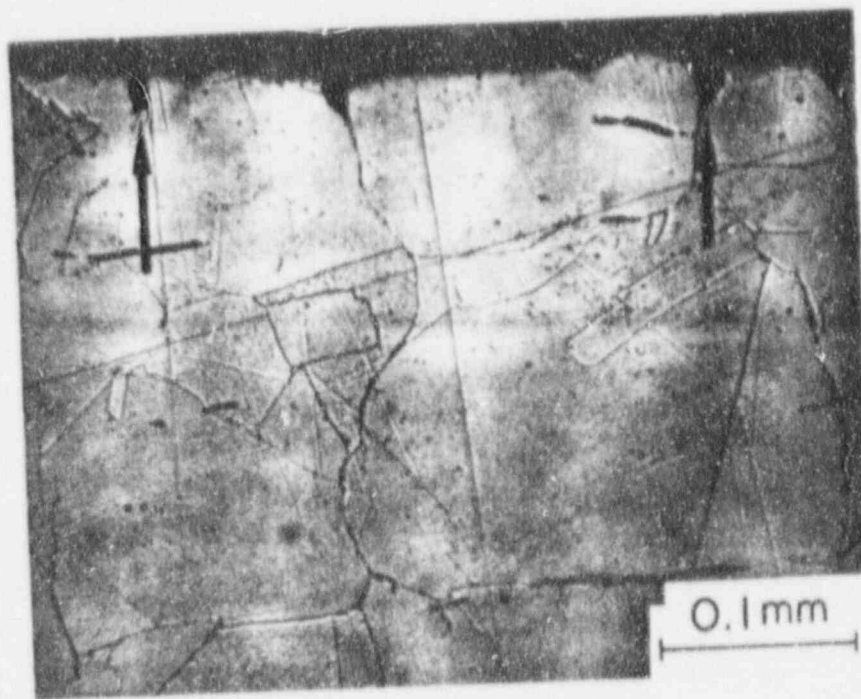
Fig. 11.   Grain structure of the elbow material.   (a) Small grains (due to recrystallization) are at the ID surface (arrow).   Large grains follow the weld fusion line.   (b) A magnified view of the ID surface.   The notching (arrow) that has occurred is seen at the grain boundaries as well as at the center of grains.
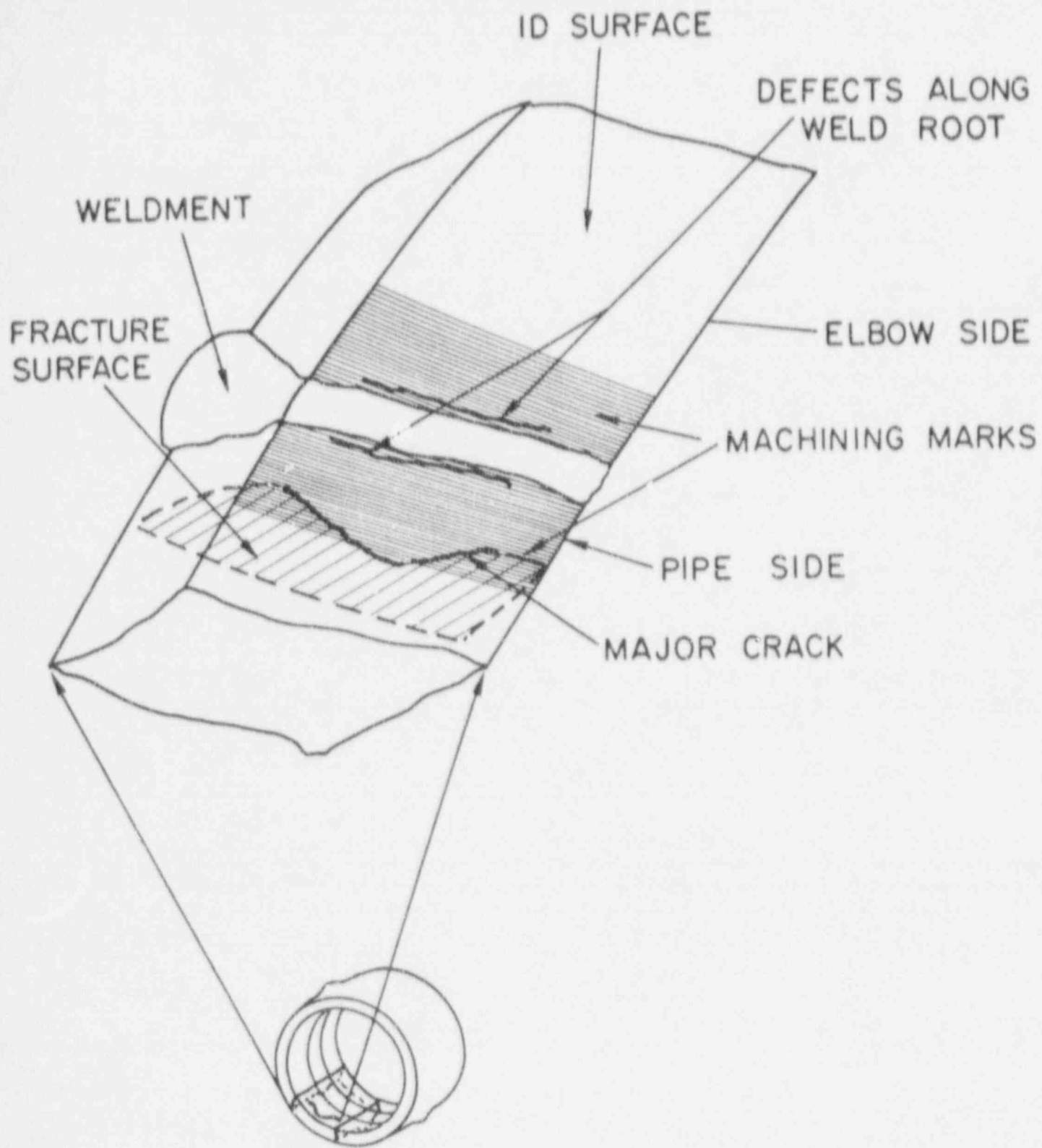
Fig. 12. Schematic diagram showing the orientation of the surface defects and major crack in relation to the pipe geometry. The fracture surface to be examined with the SEM is shown.
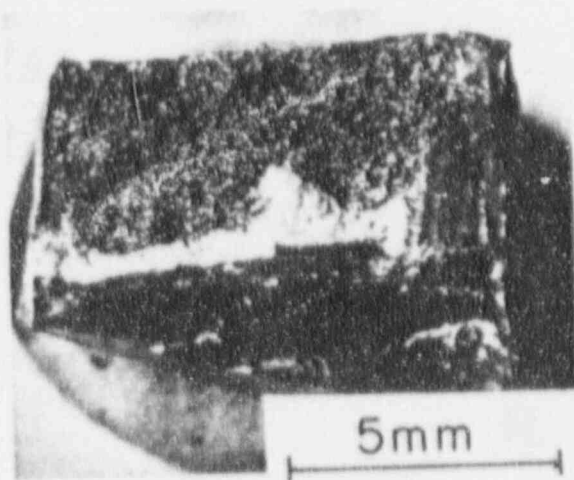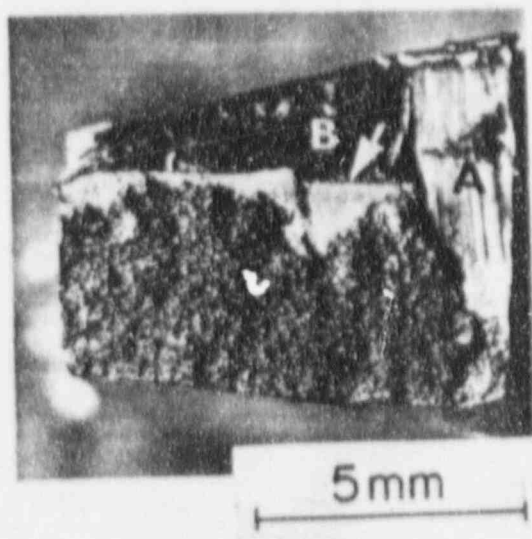
Fig. 13. The mating pieces of the fracture surface are shown. The regions labeled A and B were saw cut prior to separating the two pieces. Ductile tearing (arrow) appears as high-contrast areas on the photograph.
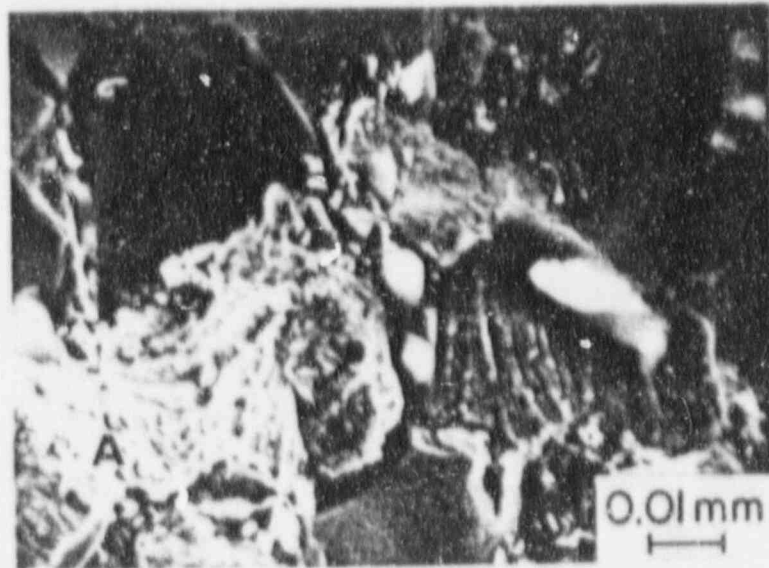
(a)
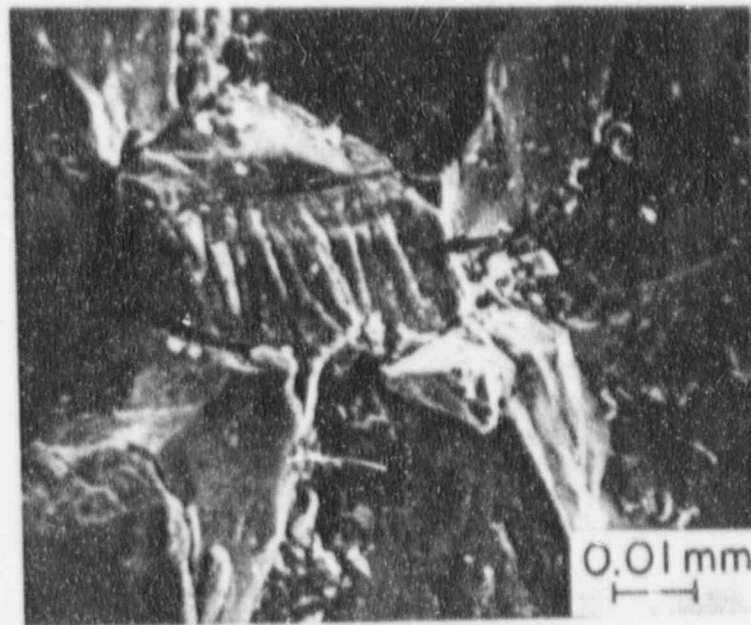
(b)

Fig. 14. The fracture surface as seen with the SEM. Photograph (a) was taken after exposure of the surface to the NS-1 solution for 100 h. Photograph (b) is the same region after 219 h in the solution. "Tongue" behavior (arrow) can be seen. These two photographs show the effects of the NS-1 solution on removing the surface oxide (A).
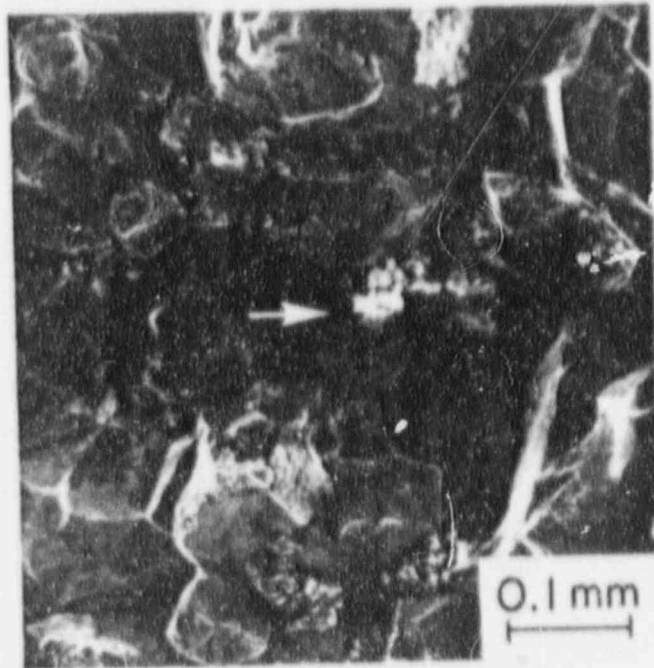
Fig. 15. An SEM photograph showing the fracture surface. The high-contrast regions are oxides that have become charged (arrow). Precipitates are also seen at the grain boundaries.
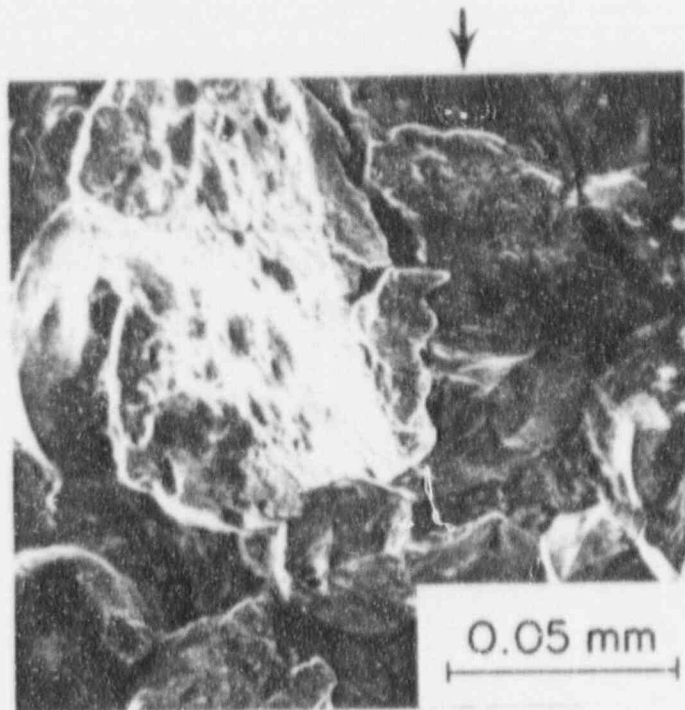
Fig. 16. Photograph showing slip (arrow).
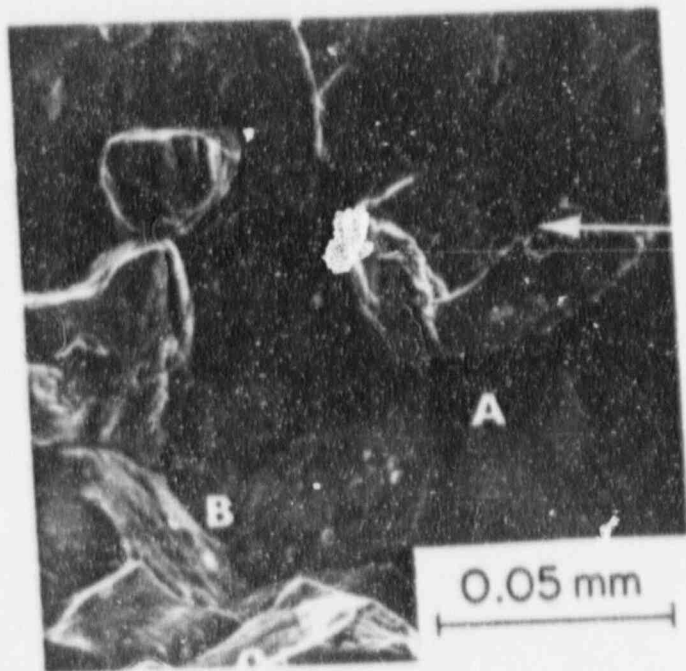
Fig. 17. Photograph showing slip (arrow),
grain-boundary separation (A),
and crack arrest (B).
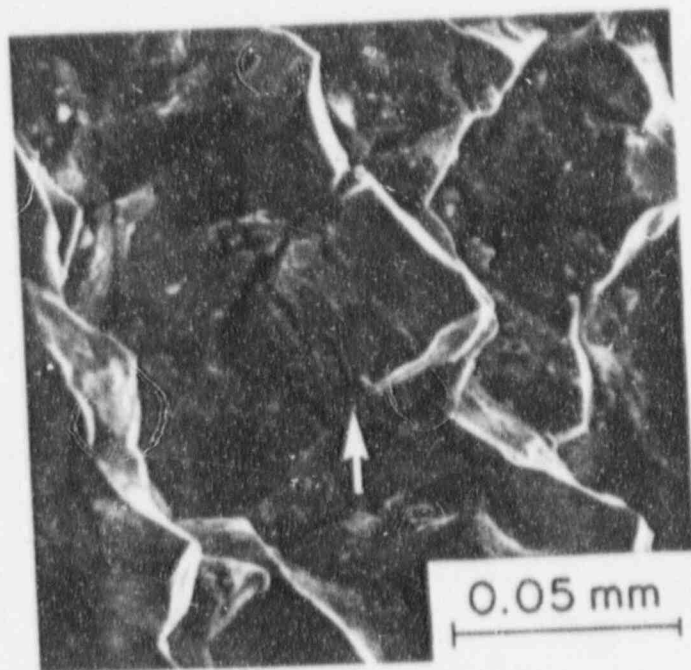
Fig. 18. Photograph showing transgranular
fracture (arrow) at an isolated
grain on the fracture surface.
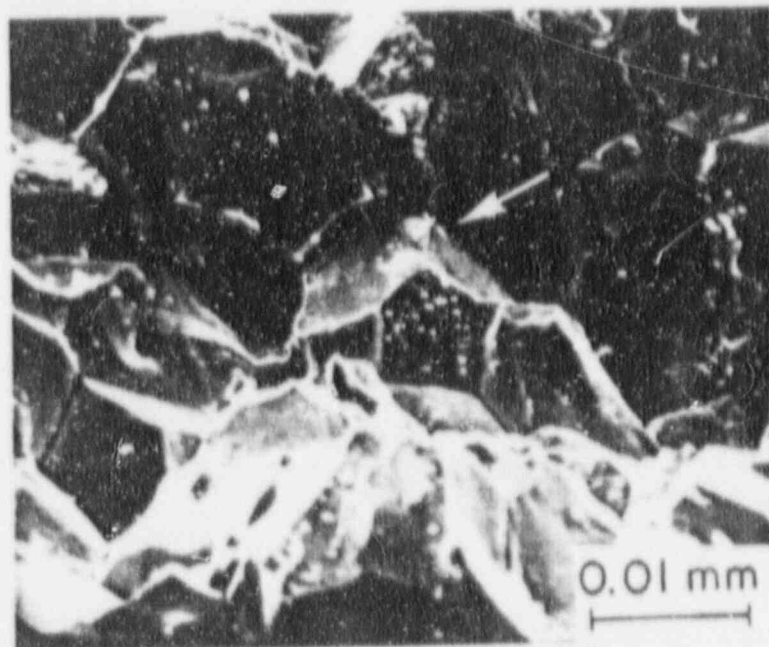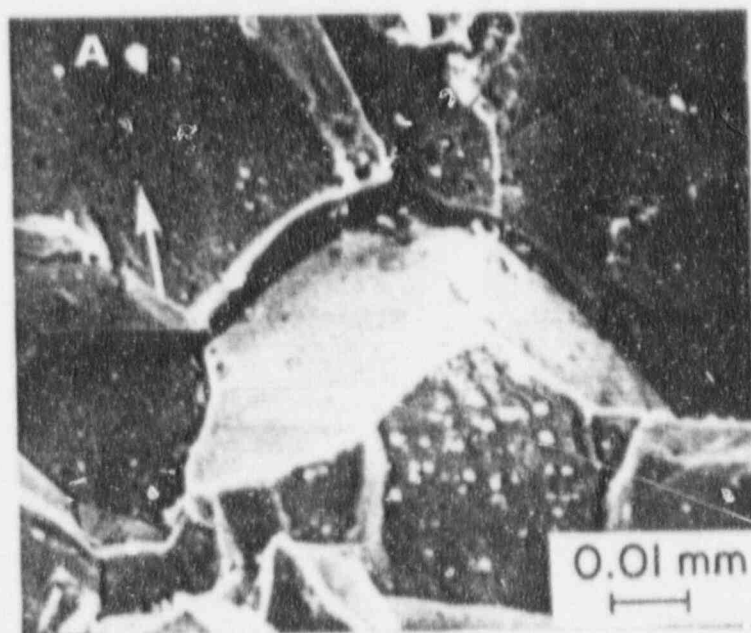
Fig. 20. (a) Crack branching, grain-boundary separation, and precipitates are shown (arrow). (b) Enlargement of (a). Dark circular areas, where precipitates had been (arrow), are seen. X-ray fluorescence was performed on precipitates bright area labelled A and the bulk grains.
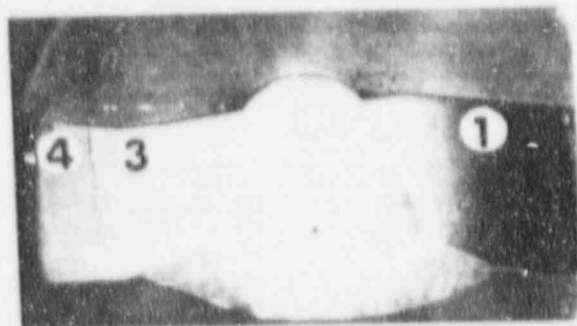
10 mm

Fig. 21. Cross-sectional view of weld RBBJ-10. The areas punched and used for TEM are numbered.
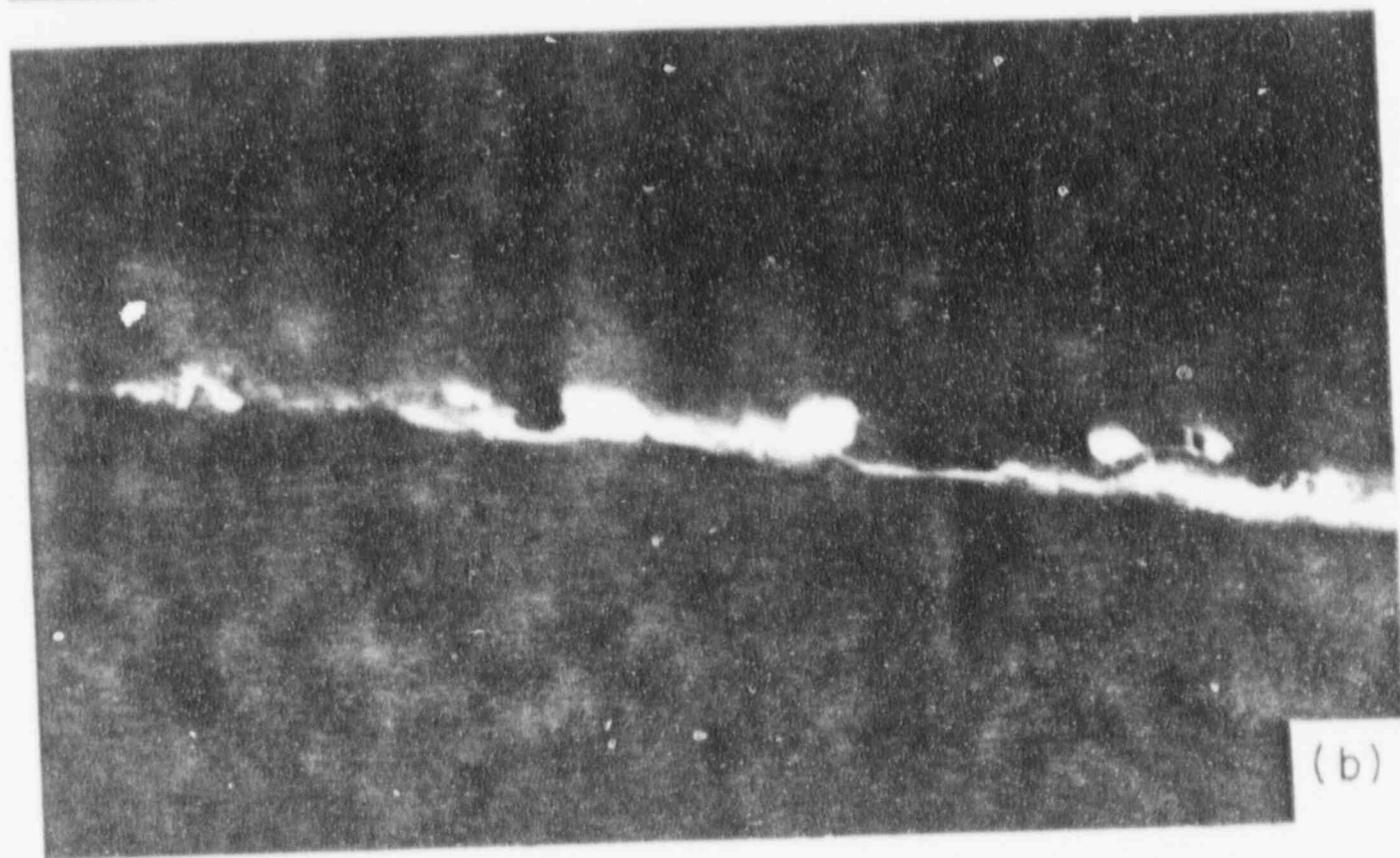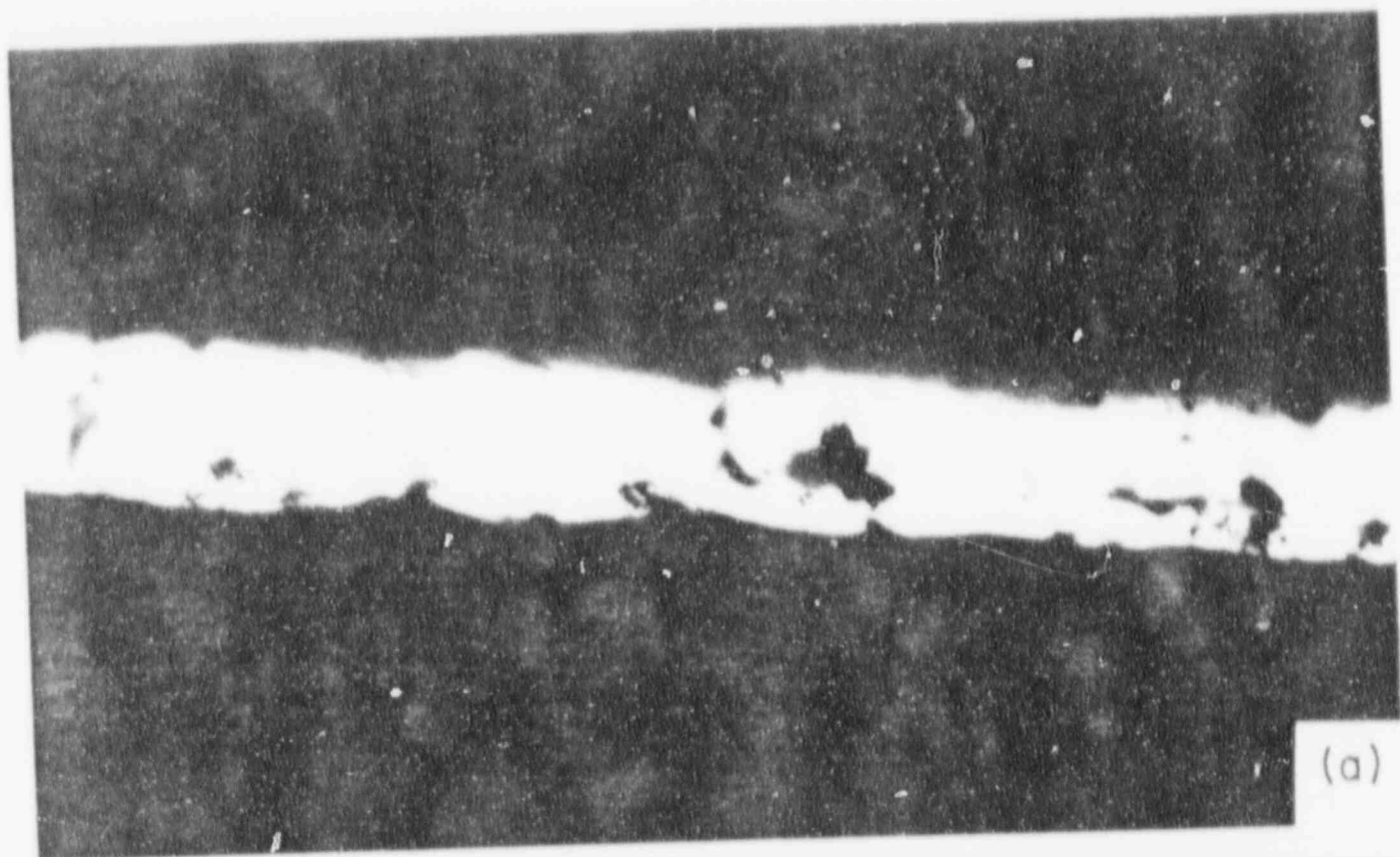
Fig. 22. Bright-field (a) and dark-field (b) TEM of a grain boundary of region 1 of Fig. 21. A grain boundary with precipitates (bright areas) is shown in (b).
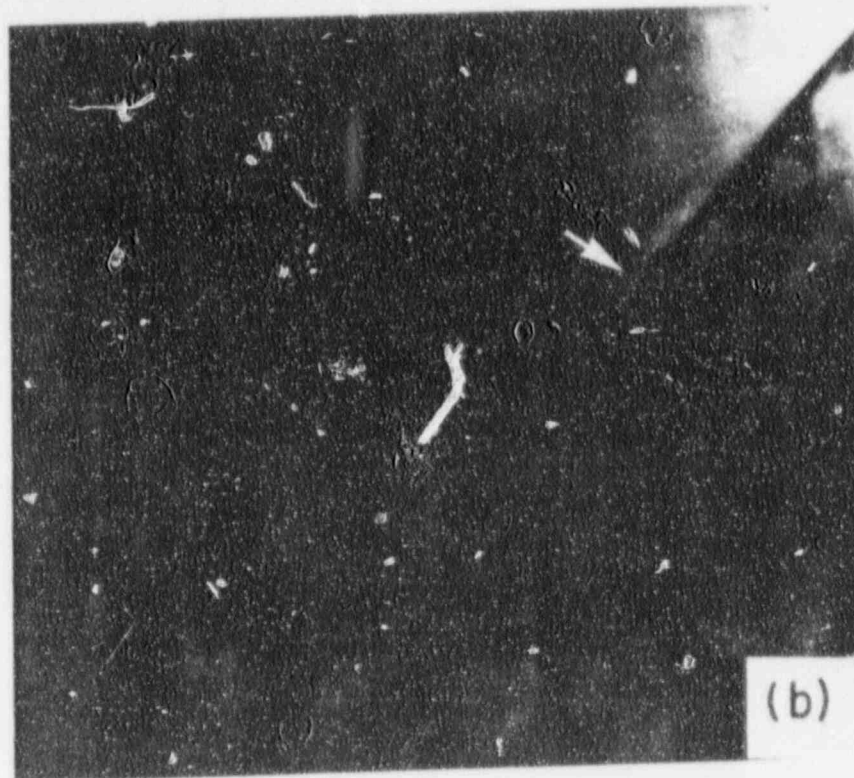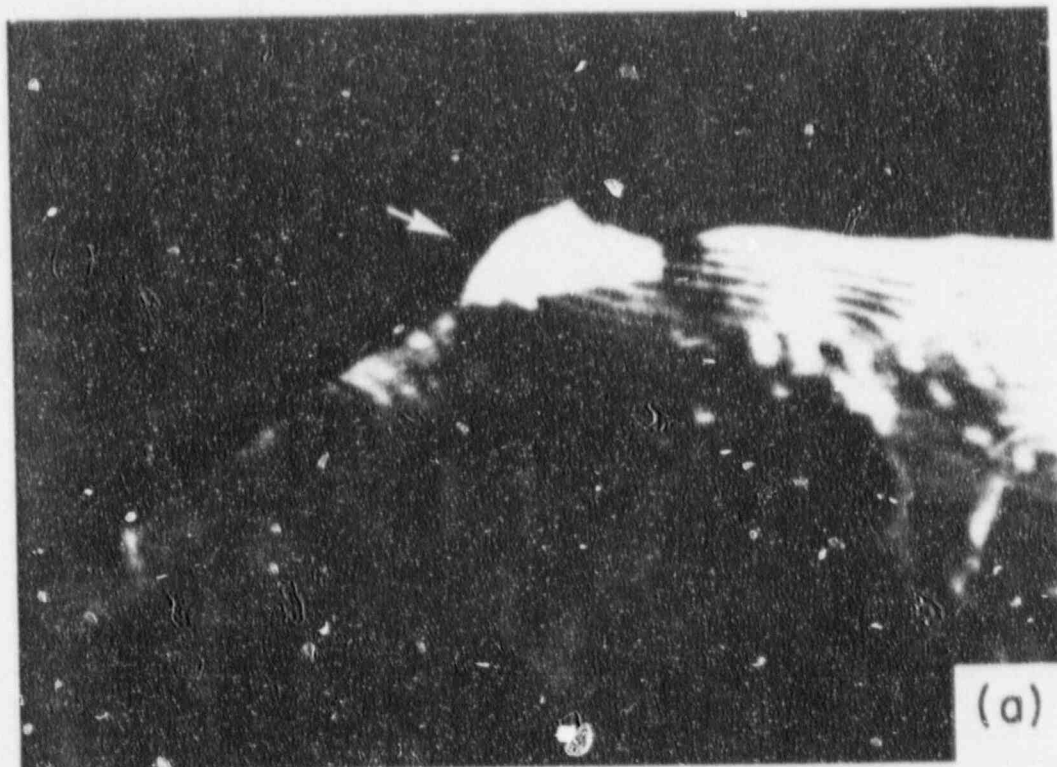
Fig. 23. Dark-field (a) and bright-field (b) TEM of a grain boundary
(arrow) of region 3 of Fig. 21. Precipitates (bright areas
in the grain boundary, (a)) are seen.
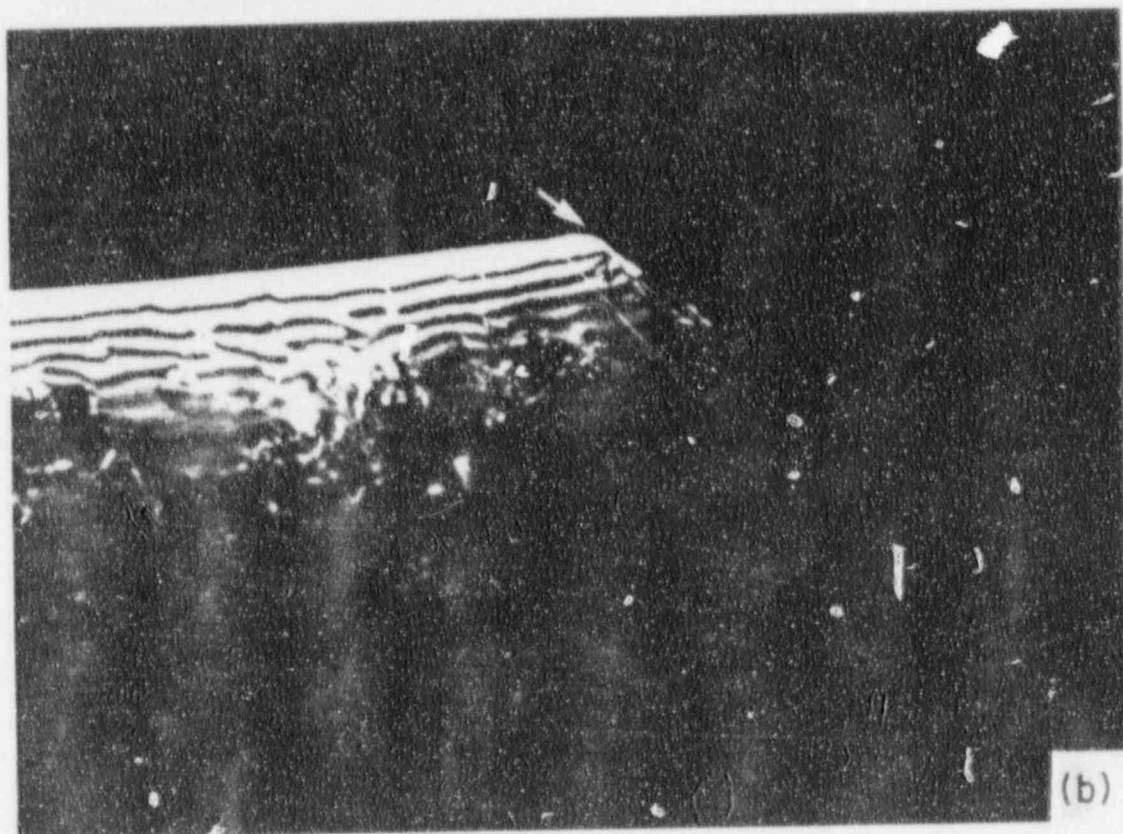
Fig. 24. Bright-field (a) and dark-field (b) TEM of a grain boundary (arrow) of region 4 of Fig. 21.
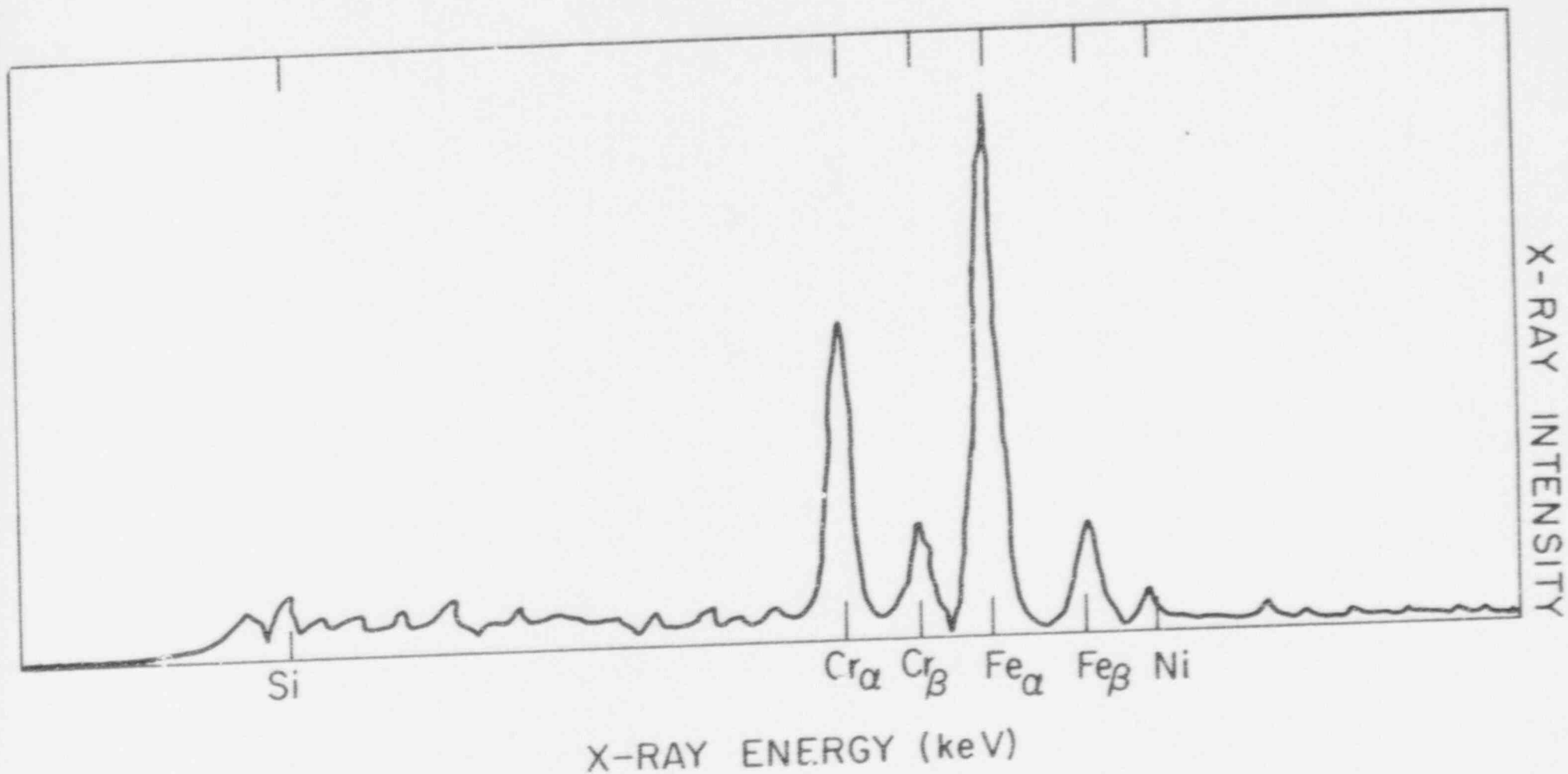
Fig. 25. X-ray fluorescence yield of the grains at the fracture surface. Si, Cr, Fe, and Ni peaks are observed. The relative magnitude of the peaks shows that the material is stainless steel.
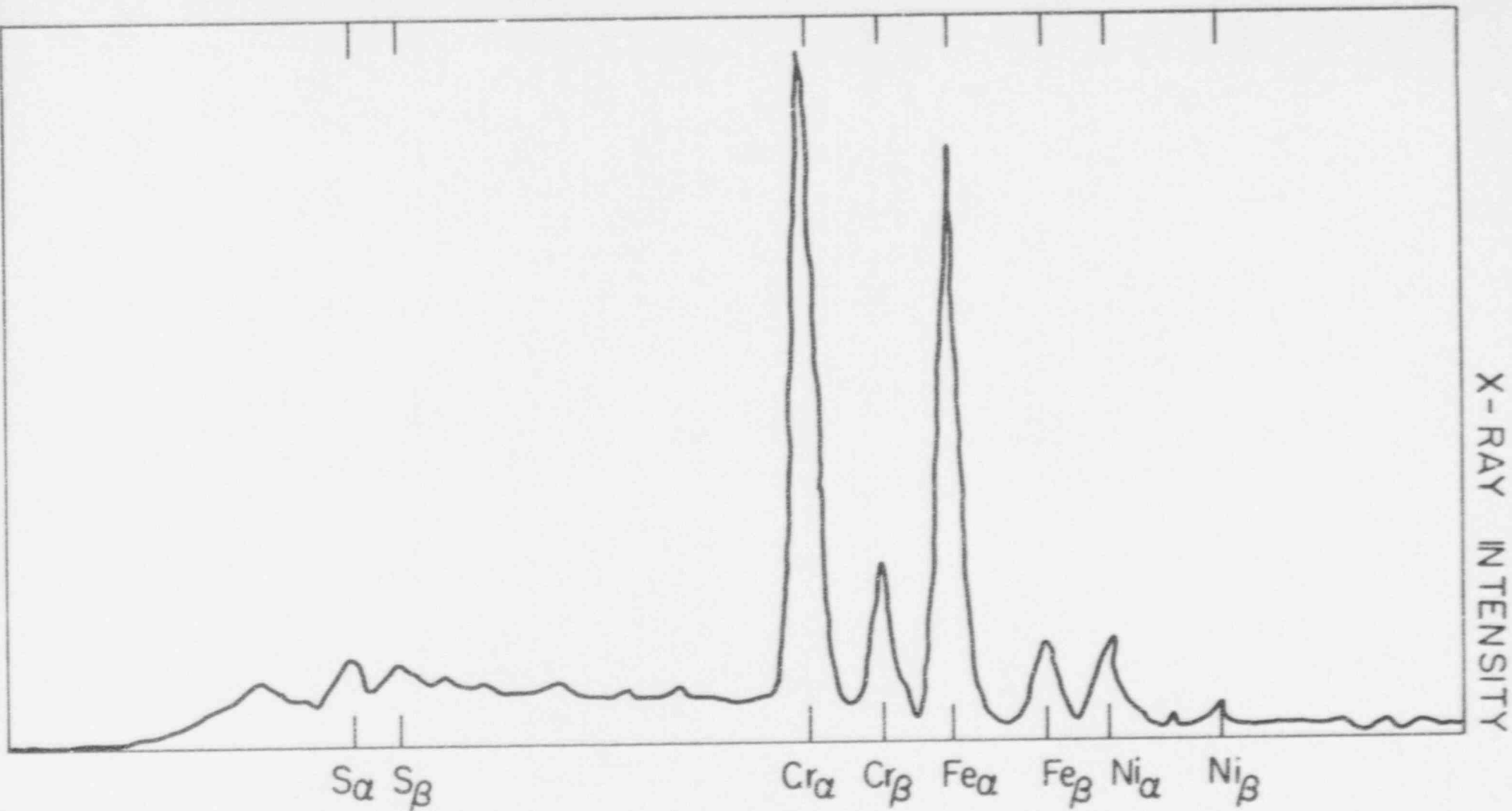
Fig. 26. X-ray fluorescence yield of a precipitate embedded in a grain boundary at the fracture surface. S, Cr, Fe, and Ni peaks are observed. The relative magnitude of the peaks (compare with Fig. 25) suggests that the particle is made of a chromium-rich spinel.

MONTICELLO
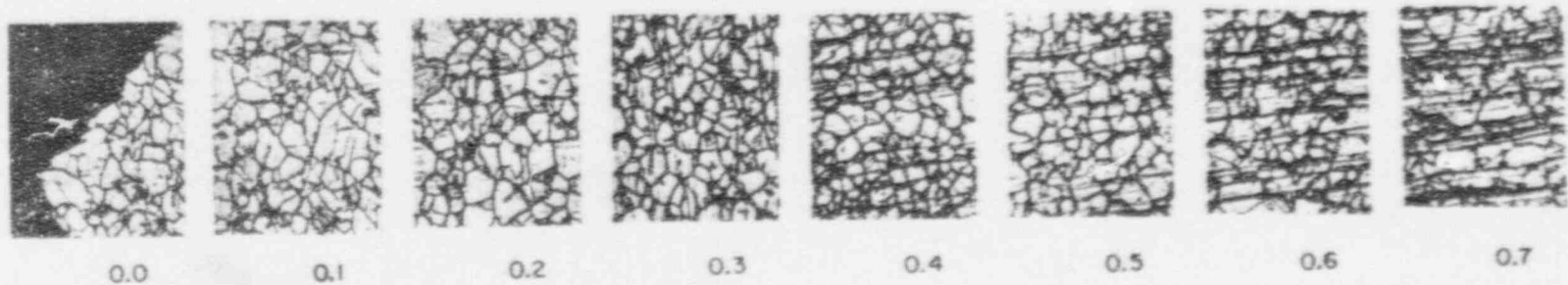LOOP B 4"

0.01"

DISTANCE
FROM WELD
FUSION LINE
(INCHES)

0.0   0.1   0.2   0.3   0.4   0.5   0.6   0.7

Fig. 27. Sensitization test of an area that includes the HAZ. The samples were immersed in
oxalic acid for a given length of time so that grain-boundary etching could occur.
The weld fusion line is shown in (a), and each succeeding photograph [(b)-(h)] is
of an area 0.1-in. farther from the weld. The heaviest sensitization is seen at a
distance of 0.4-0.5 in. from the weld. The horizontal lines are drawing lines pro-
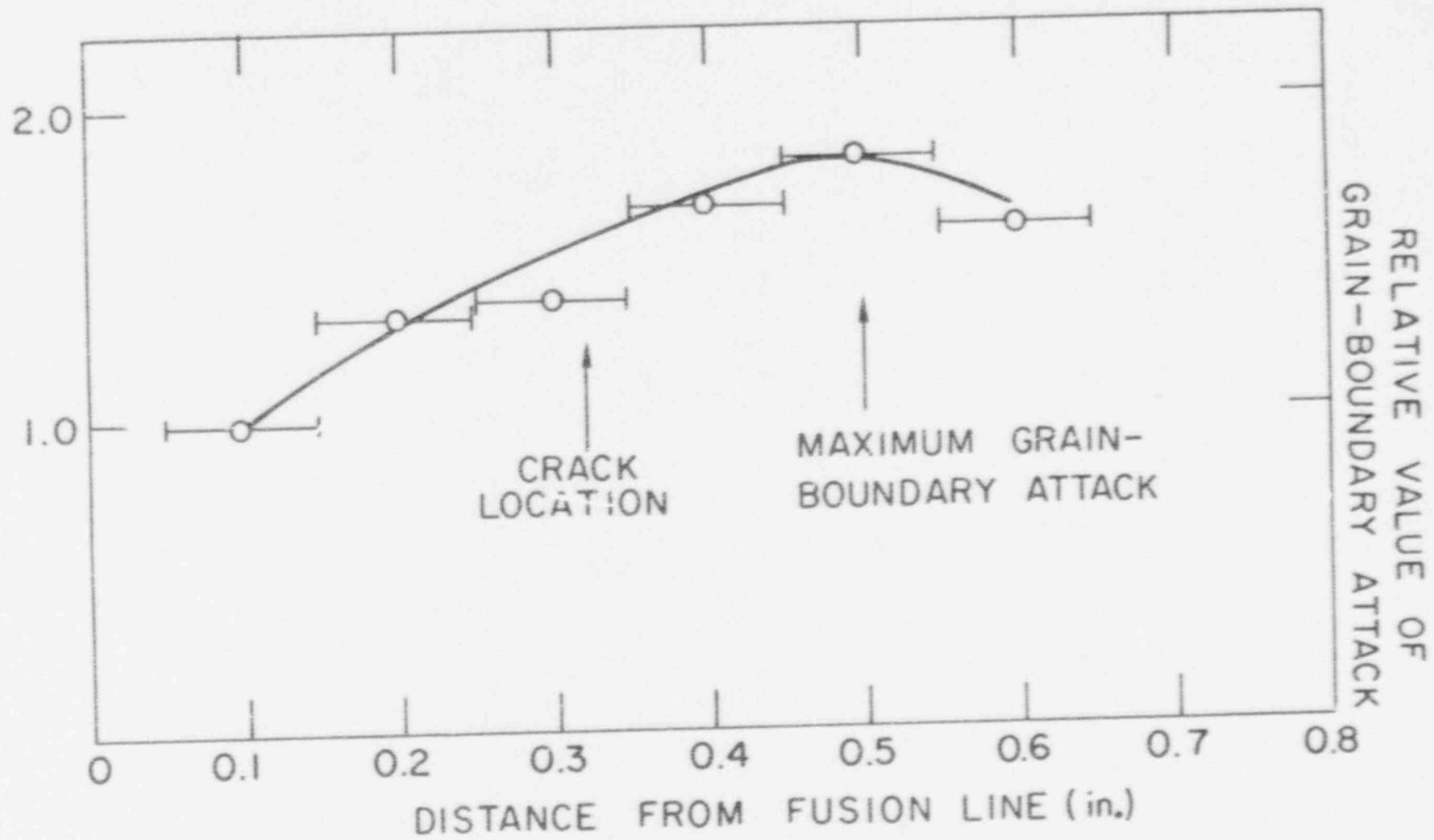duced during pipe fabrication.

Fig. 28. Relative sensitization vs distance from the fusion line. Sensitization is obtained by using the QUANTIMET scheme of measuring the relative area (dark area/light area) of etched grain boundary from Fig. 27. The maximum in sensitization occurs at 0.5 in., whereas the crack occurs 0.3 in. from the weld fusion line.
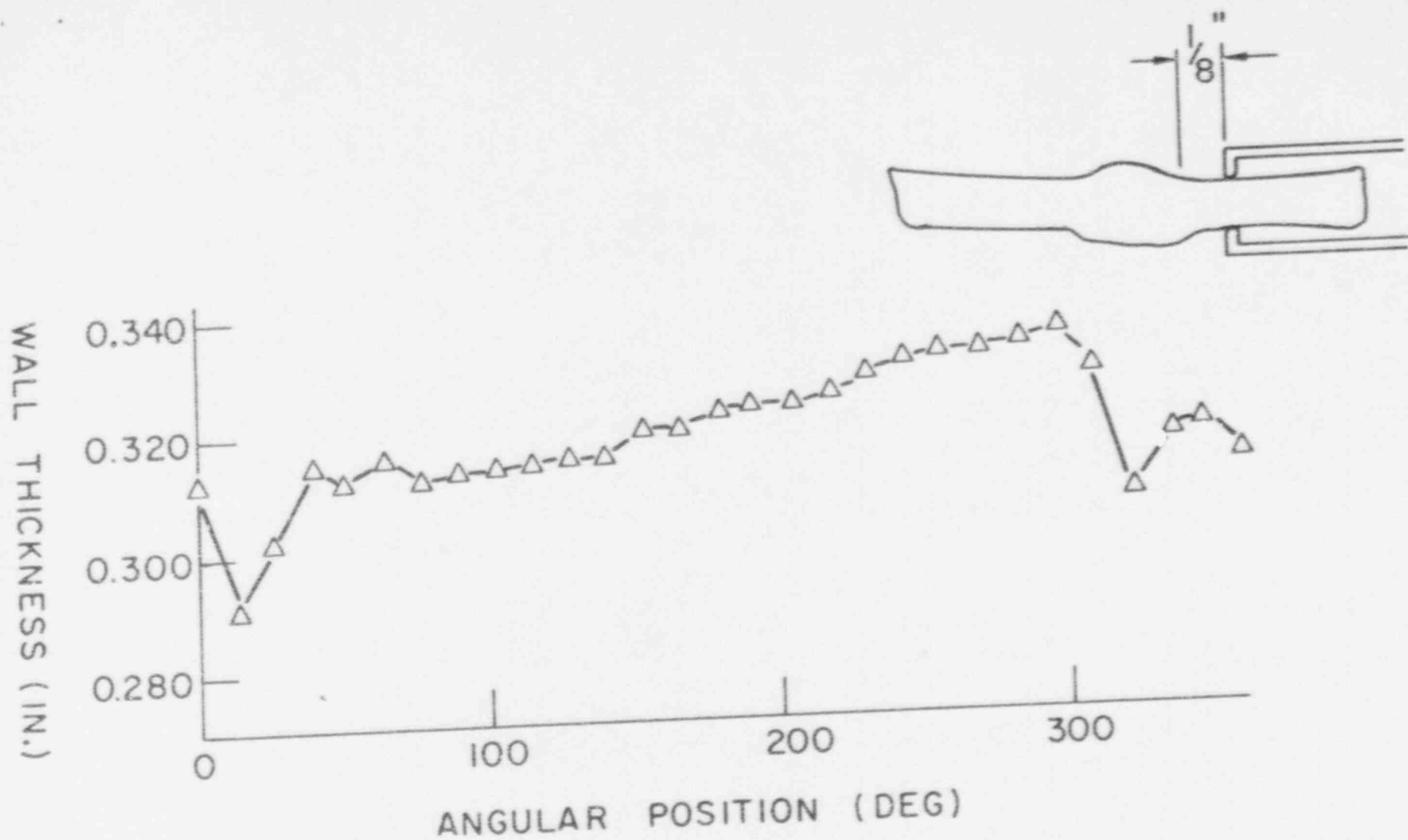
Fig. 29. Circumferential wall thickness vs angular position. The circumferential wall-thickness measurement was accomplished for weld RBAJ-7 as shown in the upper right corner of the figure. The data were obtained 1/8 in. from the weld root.
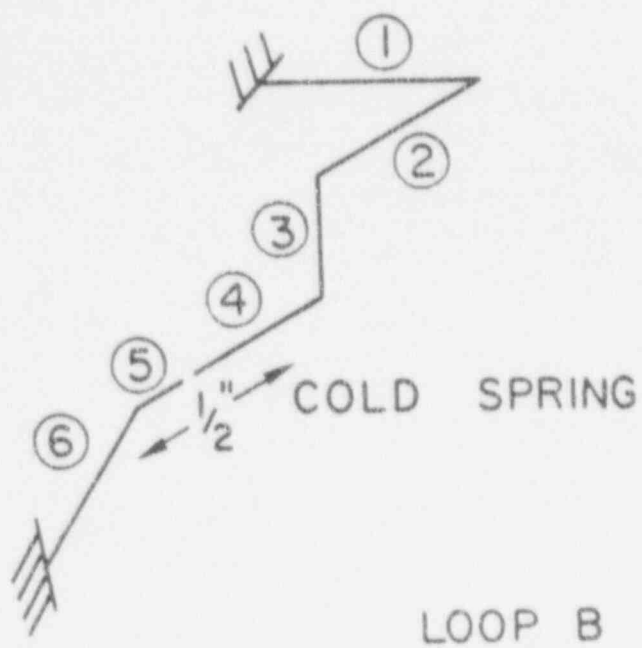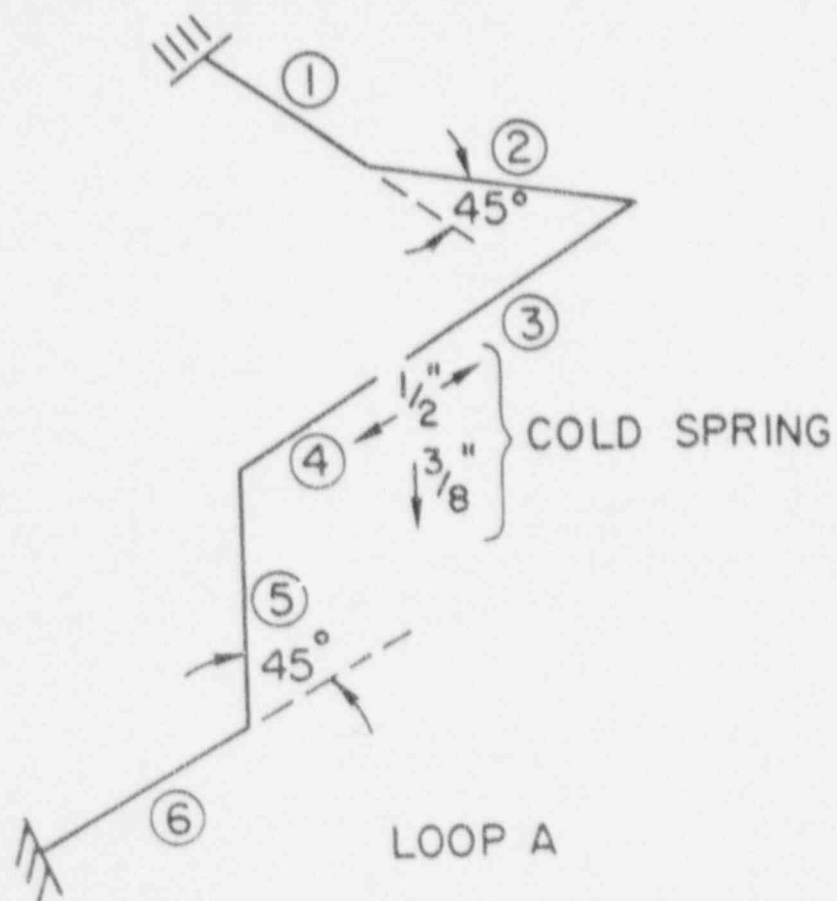
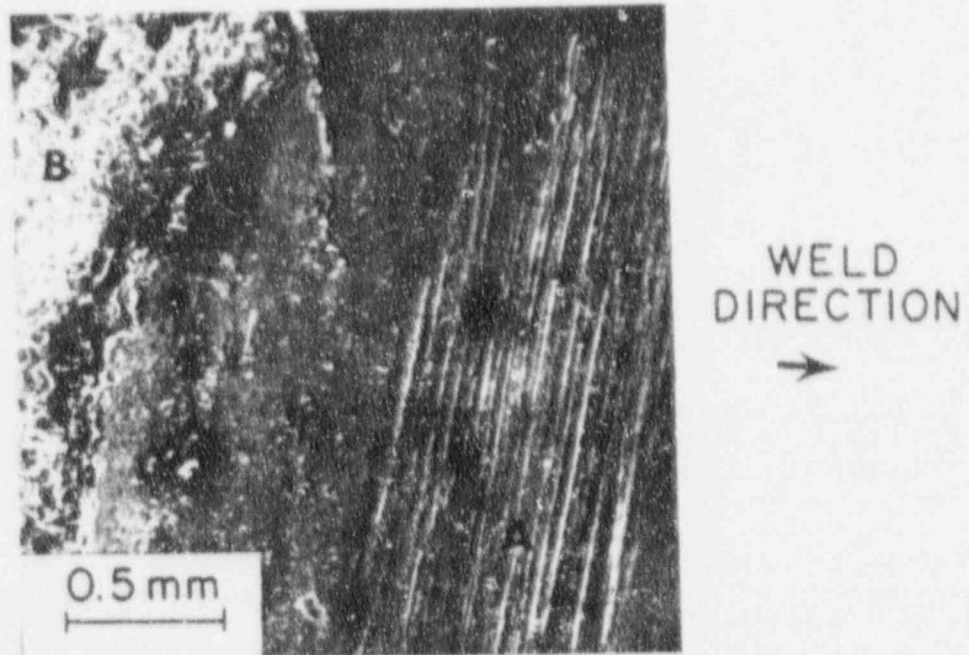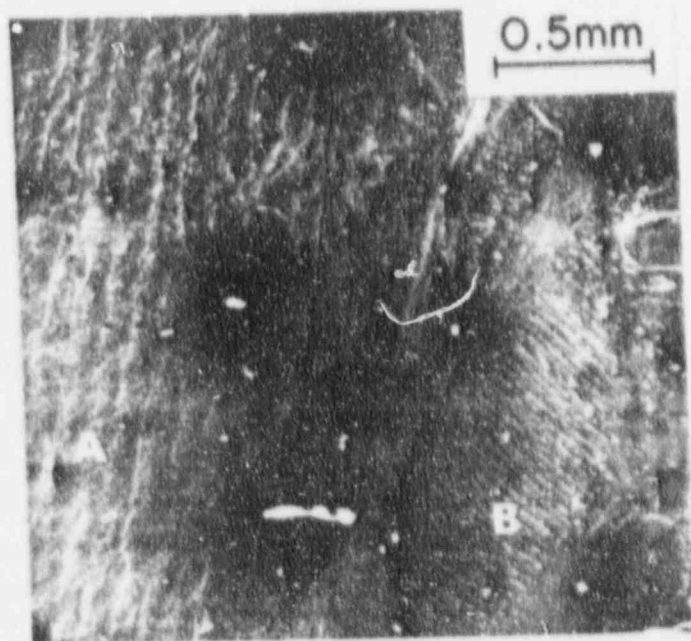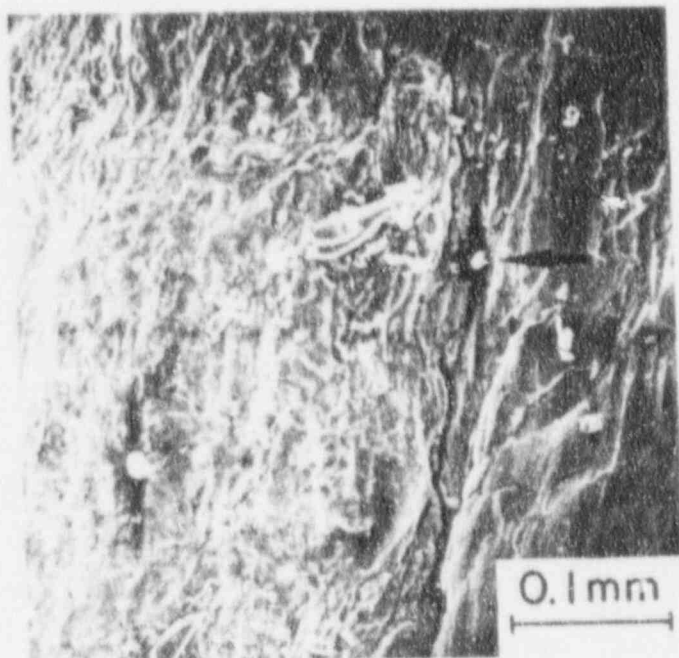Fig. 30. Schematic of cold-spring measurements.

WELD
DIRECTION
→

Fig. 31. The ID surface of RBBJ-10. The
machining marks (A) and fracture
surface (B) are seen. The crack
probably originated in a region
where machine marks exist; how-
ever, the crack edge (arrow) in
this figure is outside the
machined region.

Fig. 32. (a) The machining marks (A) and defect at the weld root are shown (arrow). The weld is at the right. Solidification marks (B) are also shown. (b) The defect at the weld root is shown magnified. The weld is at the right side of the figure. Precipitates at the grain boundaries are shown (arrow). The defect follows the weld root and is both transgranular and intergranular.